Please cite this article in press as: Ong et al., Epicardially secreted fibronectin drives cardiomyocyte maturation in 3D-engineered heart tissues, Stem Cell Reports (2023), https://doi.org/10.1016/j.stemcr.2023.03.002

Stem Cell Reports
Article
ISSCR
OPEN ACCESS

Epicardially secreted fibronectin drives cardiomyocyte maturation in 3D-engineered heart tissues

Lay Ping Ong,[1,2,6,*] Johannes Bargehr,[1,2,6] Vincent R. Knight-Schrijver,[1,2,6] Jonathan Lee,[1,2] Maria Colzani,[1,2] Semih Bayraktar,[1,2] William G. Bernard,[1,2] Silvia Marchiano,[3,4] Alessandro Bertero,[5] Charles E. Murry,[3,4] Laure Gambardella,[1,2,7] and Sanjay Sinha[1,2,7,*]

[1]Wellcome – MRC Cambridge Stem Cell Institute, Jeffrey Cheah Biomedical Centre, Cambridge Biomedical Campus, University of Cambridge, Puddicombe Way, CB2 0AW Cambridge, UK
[2]Division of Cardiovascular Medicine, University of Cambridge, Addenbrooke's Hospital, ACCI Level 6, Hills Road, Box 110, Cambridge CB2 0QQ, UK
[3]Departments of Laboratory Medicine & Pathology, Bioengineering, and Medicine/Cardiology, University of Washington, Seattle, WA, USA
[4]Center for Cardiovascular Biology, Institute for Stem Cell and Regenerative Medicine, University of Washington, Seattle, WA, USA
[5]Molecular Biotechnology Center, Department of Molecular Biotechnology and Health Sciences, University of Torino, Via Nizza 52, 10126 Torino, Italy
[6]These authors contributed equally
[7]These authors contributed equally
*Correspondence: lpo20@cam.ac.uk (L.P.O.), ss661@cam.ac.uk (S.S.)
https://doi.org/10.1016/j.stemcr.2023.03.002

SUMMARY

Ischemic heart failure is due to irreversible loss of cardiomyocytes. Preclinical studies showed that human pluripotent stem cell (hPSC)-derived cardiomyocytes could remuscularize infarcted hearts and improve cardiac function. However, these cardiomyocytes remained immature. Incorporating hPSC-derived epicardial cells has been shown to improve cardiomyocyte maturation, but the exact mechanisms are unknown. We posited epicardial fibronectin (FN1) as a mediator of epicardial-cardiomyocyte crosstalk and assessed its role in driving hPSC-derived cardiomyocyte maturation in 3D-engineered heart tissues (3D-EHTs). We found that the loss of FN1 with peptide inhibition F(pUR4), CRISPR-Cas9-mediated FN1 knockout, or tetracycline-inducible FN1 knockdown in 3D-EHTs resulted in immature cardiomyocytes with decreased contractile function, and inefficient Ca^{2+} handling. Conversely, when we supplemented 3D-EHTs with recombinant human FN1, we could recover hPSC-derived cardiomyocyte maturation. Finally, our RNA-sequencing analyses found FN1 within a wider paracrine network of epicardial-cardiomyocyte crosstalk, thus solidifying FN1 as a key driver of hPSC-derived cardiomyocyte maturation in 3D-EHTs.

INTRODUCTION

The global burden of heart failure is reflected by an estimated 37.7 million patients, of whom 50% will not survive the 5 years following their diagnosis (Ziaeian and Fonarow 2016; Zarrinkoub et al., 2013). A large proportion of heart failure is due to ischemic myocardial injury resulting in loss of contractile working myocardium. The only curative therapeutic option is heart transplantation, which is substantially hampered by a severe shortage of donor organs. Regenerative cardiovascular medicine has the potential to address the loss of contractile function by remuscularizing the failing heart. Indeed, transplantation of human pluripotent stem cell (hPSC)-derived CMs (CMs) results in formation of robust cardiac grafts in rodents (Laflamme et al., 2007; Shiba et al., 2013) and non-human primates (Chong et al., 2014; Shiba et al., 2016), and improves cardiac function (Liu et al., 2018). Aside from direct intramyocardial cell injection, an alternative approach is to generate 3D-engineered heart tissues (3D-EHTs) to be transplanted on the epicardial heart surface (Weinberger et al., 2016; Tiburcy et al., 2017).

Current shortcomings limiting the efficiency of hPSC-based therapeutic applications include hPSC-CM immaturity, lack of vascular supply, and limited CM proliferation following engraftment, resulting in suboptimal function and tissue repair. The generation of cardiovascular tissues with enhanced structure and function will aid in overcoming these limitations. In this context, the epicardium is known as an essential embryonic source of cardiac fibroblasts and coronary smooth muscle cells, which contribute to the formation of the extracellular niche and the coronary vasculature, respectively (Guadix et al., 2006; Gittenberger-de Groot et al., 1998). Recently we have demonstrated that human embryonic stem cell (hESC)-derived epicardial cells (EPIs) promote hESC-CM structural and functional maturity both *in vitro* in 3D-EHTs and *in vivo* in infarcted athymic rats, improving cardiac function and graft vascularization following transplantation (Bargehr et al., 2019).

Despite directing critical parts of cardiac development (Gittenberger-de Groot et al., 1998), the epicardial-myocardial crosstalk remains largely unelucidated. An analysis of the hESC-EPI secretome has provided an initial insight into factors implicated in these regenerative processes, highlighting the potential role of fibronectin (FN1) (Bargehr et al., 2019). In zebrafish, animals capable of cardiac regeneration, epicardial FN1 is required for repair following cardiac injury (Wang et al., 2013). Furthermore, FN1 is known to regulate key processes during development and disease, including growth, proliferation, migration, and survival (Schwarzbauer and DeSimone 2011;

Please cite this article in press as: Ong et al., Epicardially secreted fibronectin drives cardiomyocyte maturation in 3D-engineered heart tissues, Stem Cell Reports (2023), https://doi.org/10.1016/j.stemcr.2023.03.002

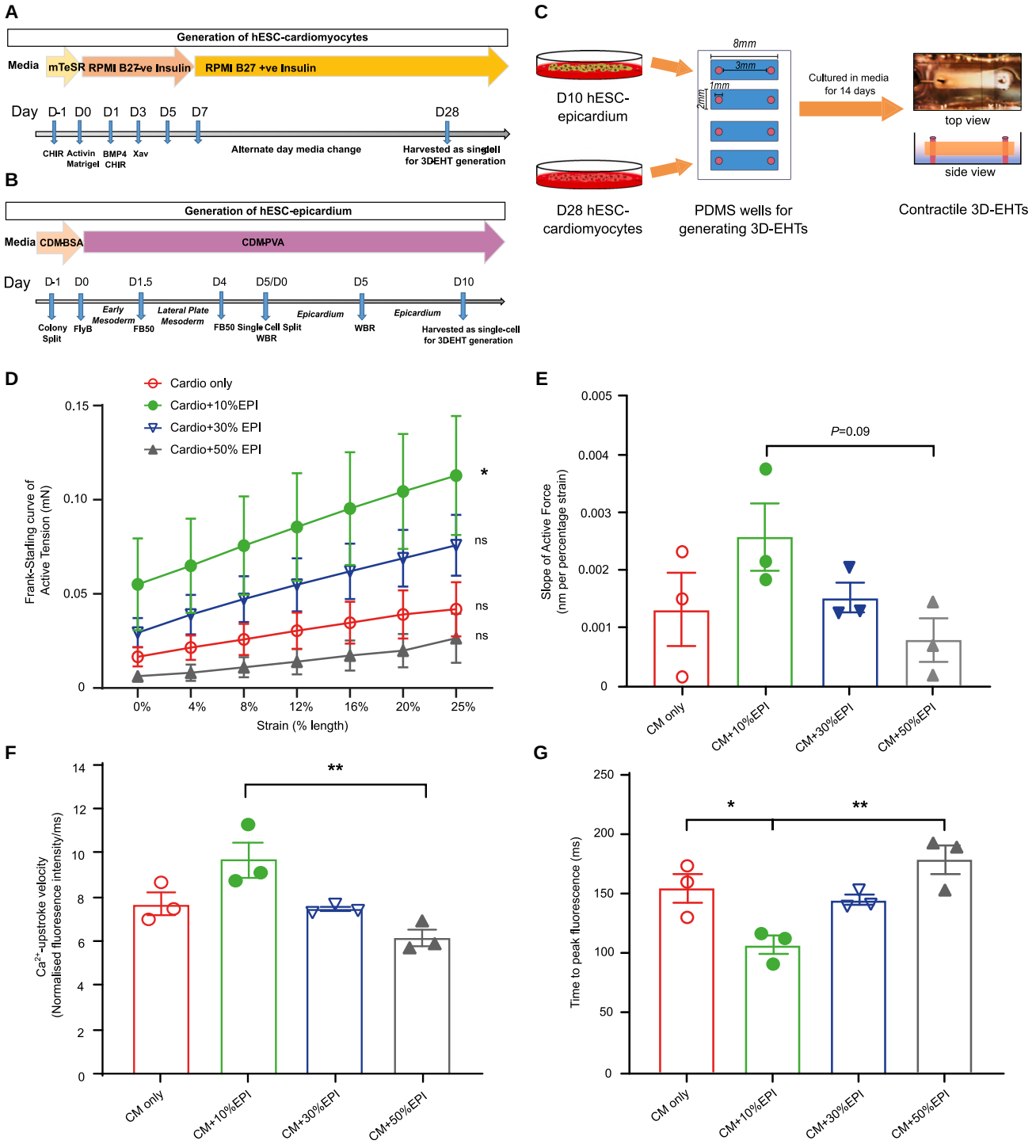

Figure 1. Generation of 3D-EHTs with optimized cell ratios

(A) Schematic for derivation of hESC-CMs.

(B) Schematic for derivation of hESC epicardium.

(C) Schematic for the generation of collagen-based 3D-EHTs containing hESC-CMs and EPIs and their subsequent histological and functional assessment.

(D) Frank-Starling curves of active force generation of 3D-EHTs containing CM only, CM + 10% hESC epicardium, CM + 30% hESC epicardium, or CM+50% hESC epicardium.

(legend continued on next page)

Mittal et al., 2010; Astrof et al., 2007). The embryonic identity of EPIs is critical in this process as embryonic but not adult cardiac fibroblasts can induce CM proliferation via FN1 (Ieda et al., 2009). Given the fetal identity of hESC-EPIs (Knight-Schrijver et al., 2022), we hypothesized that epicardial FN1 serves a functional role in CM development and maturation from hESCs comparable with the one seen in the developing myocardium.

Here we demonstrate the potent role of epicardial FN1 as an enhancer of CM structure and function in 3D-EHTs. We show that loss of epicardial FN1 function, first through pharmacological inhibition with pUR4, an inhibitor of FN1- integrin $\alpha5\beta1$ binding, second through constitutive loss following CRISPR-Cas9-mediated FN1 knockout (KO), and third following tetracycline-inducible FN1 knockdown (sOPTiKD), consistently results in an impaired ability of the epicardium to promote hESC-CM maturity. A lack of epicardial FN1 deposition in 3D-EHTs results in compromised hESC-CM maturity, as demonstrated by reduced myofibril alignment, shortened sarcomeric length, impaired Ca^{2+}-kinetics, and a reduction in active force generation. To further investigate the EPI-CM crosstalk, we generate the interactome of hESC-EPI and hESC-CM using RNA bulk sequencing and reveal a unique signaling network governing myocardial growth and maturation in which FN plays a key role. These data highlight the role of FN as a key mediator of epicardial-driven growth and maturation, by assigning FN1 a vital role in the hESC-derived EPI-CM crosstalk; the analysis of which reveals signaling pathways that can be exploited to further advance regenerative cardiac applications.

RESULTS

Competitive inhibition of FN1 using the recombinant peptide pUR4 impairs hESC-CM maturation

To study the effects of epicardial FN1 on CM structure and function, we first generated 3D-EHTs with hESC-CMs and hESC-EPIs (Figures 1A–1C). For each experiment, 3D-EHTs were transferred to a myograph with a length controller and a force transducer to assess force generation followed by testing of Ca^{2+} kinetics. We also assessed CM structure using histological sections.

Before investigating the effects of FN1 inhibition, we optimized the ratio of CM and EPI cells within the 3D-EHTs and found that 3D-EHTs containing 10% EPI generated the greatest amount of active and passive force compared with 3D-EHTs containing either 30% EPI or 50% EPI, or only CM (Figures 1D, 1E, S1A, and S1B). We confirmed this result by investigating Ca^{2+} handling and found the highest Ca^{2+}-upstroke velocity, shortest time to peak, and shortest decay time in 3D-EHTs containing 10% EPI (Figures 1F, 1G, S1C, and S1D).

To test whether epicardial FN1 was at least in part responsible for the epicardial effects on CM structure and function, we inhibited FN1 using the 49-residue recombinant peptide pUR4. pUR4 binds to the N-terminal regions of FN1, competing with $\alpha5\beta1$ for its binding domain and inhibiting assembly of FN fibrils (Figure 2A). We treated our hESC-EPI in 2D monolayers with pUR4 for 72 h and noted that FN1 protein levels in the cell/substrate layer were drastically reduced (Figure 2B). Furthermore, using immunohistochemistry (IHC) we found that FN1 deposition was qualitatively and quantitatively reduced in 3D-EHTs composed of pUR4-treated EPI cells compared with constructs containing untreated EPI (Figures 2C and 2D). This finding was consistent with diminished $\alpha5\beta1$ clustering (Figures 2E and S1E) and paralleled by reduced sarcomeric length and myofibril alignment of CMs in 3D-EHTs containing pUR4-treated EPI (Figures 2F and 2G).

We next assessed active and passive force generation on a myograph and found that the active force generated by 3D-EHTs was significantly reduced when pUR4-treated EPI cells were used in their construction compared with untreated EPI (Figures 2H and 2I). However, pUR4-mediated inhibition of epicardial FN1 had no effect on passive force generated by 3D-EHTs (Figures 2J and 2K). Finally, we also examined Ca^{2+} handling, which showed that FN1 inhibition reduced Ca^{2+} upstroke velocity and increased times to peak fluorescent intensity of 3D-EHTs, but not decay times (Figures 2L–2O).

In summary, the performance of 3D-EHTs was impaired after inhibiting FN1-integrin binding, suggesting that intact fibrillogenesis of FN1 is an essential component of the epicardial effect on promoting structure and function of CMs.

Constitutive loss of epicardial FN1 using a CRISPR-Cas9-edited KO hESC line impairs CM maturation

To study the effects of a complete loss of epicardial FN1 from the hESC stage onwards, we generated a

(E) Slope of active force generation.
(F) Ca^{2+}-upstroke velocity of 3D-EHTs containing CM only, CM + 10% hESC epicardium, CM + 30% hESC epicardium, or CM + 50% hESC epicardium.
(G) Time to peak Ca^{2+}-fluorescence in 3D-EHTs containing CM only, CM + 10% hESC epicardium, CM + 30% hESC epicardium, or CM + 50% hESC epicardium.
(F and G) Presented calcium cycling data were taken from constructs paced at 1 Hz. Data presented as mean values; error bars represent SEM. *p < 0.05, **p < 0.005, ***p < 0.0001. Two-sided p values were calculated using a one-way ANOVA with *post hoc* correction for multiple comparisons. Each experimental group included N = 3 biological replicates.

Please cite this article in press as: Ong et al., Epicardially secreted fibronectin drives cardiomyocyte maturation in 3D-engineered heart tissues, Stem Cell Reports (2023), https://doi.org/10.1016/j.stemcr.2023.03.002

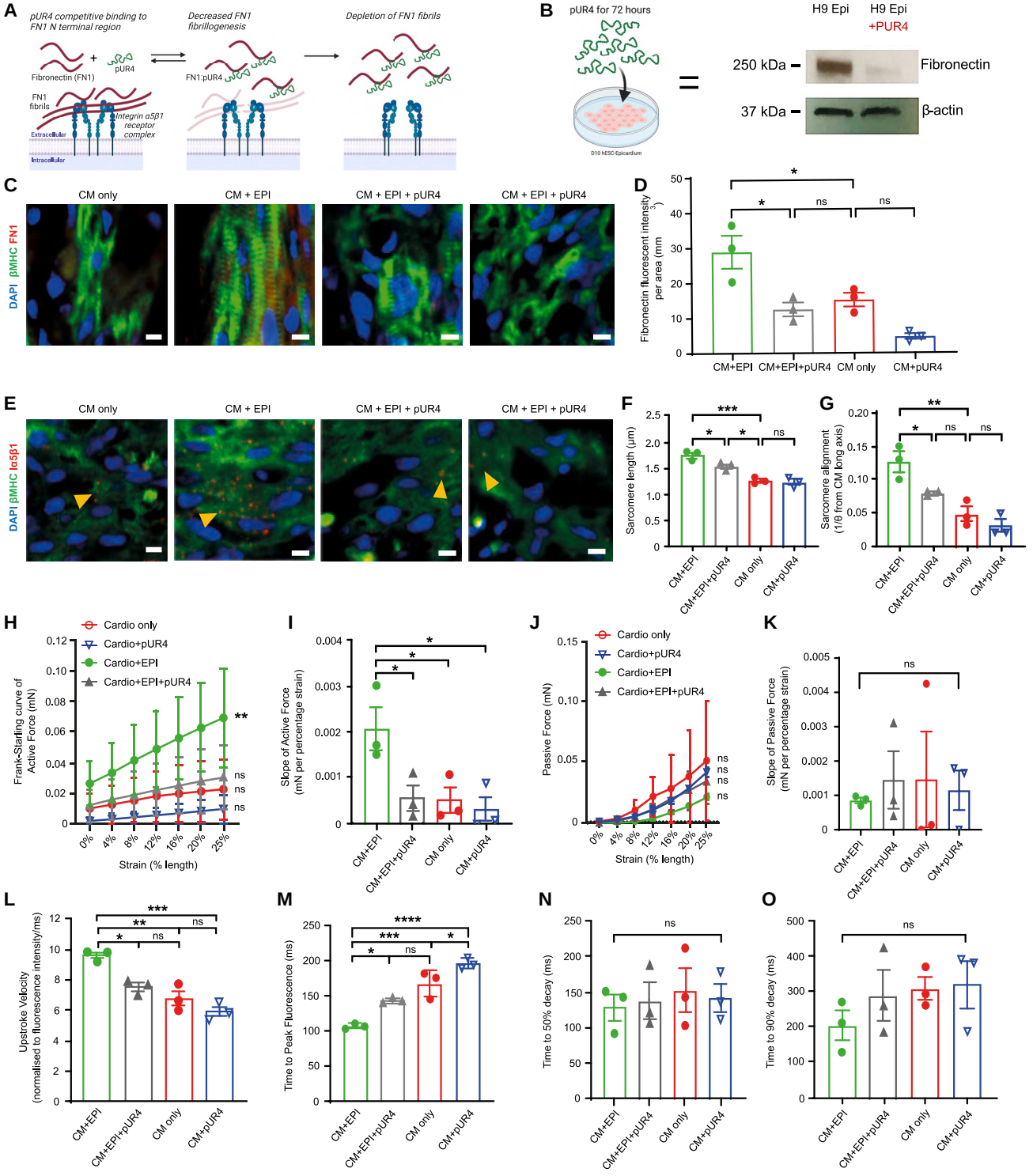

Figure 2. Pharmacological inhibition of epicardial FN1 with pUR4 results in impaired FN1 binding to integrin α5β1 and reduced CM maturation

(A) Schematic describing the mechanism of action of the recombinant peptide pUR4. PUR4 prevents FN1 from binding to the cell surface receptor integrin α5β1, hence preventing FN fibrillogenesis and signal transduction.

(B) Marked reduction of FN1 expression at the protein level 72 h post treatment of hESC epicardium with pUR4.

(legend continued on next page)

CRISPR-Cas9-edited FN1 KO line from RUES2 hESCs (KOFN1) (Figures S2A–S2C). We first showed that KOFN1-hESCs can differentiate to EPIs, as demonstrated by robust expression of the epicardial markers *WT1*, *TCF21*, and *BNC1* at the transcript and protein level, respectively (Figures 3A and 3B). At the same time KOFN1-EPI completely lacked FN1 expression both at the transcript and protein level, in contrast with wild-type (WT) EPI (Figures 3C and 3D). In 3D-EHTs containing KOFN1-EPI, FN1 deposition was also markedly reduced and clustering of integrin α5β1 was impaired (Figures 3E–3G and S2D). These results demonstrated a successful loss of FN1 in our constructs while epicardial identity was maintained, allowing us to focus on FN1-specific effects.

Using the same assessments as before, we examined how a constitutive loss of FN1 in EPI-containing 3D-EHTs affects CM structure and function. First, we found that CMs in constructs containing KOFN1-EPI had shorter sarcomeric lengths and a reduced myofibril alignment compared with CMs in constructs containing WT-EPI (Figures 3H and 3I). In line with these findings, the inclusion of KOFN1-EPI in 3D-EHTs instead of WT-EPI attenuated the active force-length relationship, while no effects on passive force generation were observed (Figures 3J–3M). This was paralleled by decreased Ca^{2+} upstroke velocity and increased time to peak fluorescence (Figures 3N and 3O), but not a significant prolongation of Ca^{2+} decay times (Figures 3P and 3Q). Finally, we noted high variance in Ca^{2+} handling data in experiments shown in Figures 1, 2, and 3 with inconsistencies in differences between the control conditions in individual experiments (hESC-CM only compared with hESC-CM + EPI) (Figures 1F, 1G, S1C, S1D, 2L–2O, 3P, and 3Q). However, we pooled the results of these control conditions together and the differences reached statistical significance, validating our experiments (Figure S4G).

Collectively, these results corroborated our findings on FN1 inhibition, demonstrating that a complete loss of epicardial FN1 in 3D-EHTs impaired CM maturation and produced CMs with a structure and function comparable with CMs in 3D-EHTs constructed without any EPI.

Temporal loss of epicardial FN1 expression with a tetracycline-inducible knockdown is sufficient to abrogate CM maturation

To investigate the effects of temporal modulation of epicardial FN1 expression, we performed a tetracycline-inducible knockdown (KD) of FN1. For this we made use of a single-step optimized inducible gene KD (sOPTiKD) of *FN1* to generate an hESC-sOPTiKD-FN1 cell line (Bertero et al., 2016, 2018) (Figures S3A–S3C). We then differentiated three sOPTiKD-FN1 H9 clones into hESC-EPI, which expressed epicardial markers including FN1 and maintained typical epicardial morphology (Figures 4A–4C). All clones successfully downregulated *FN1* after exposure to tetracycline (up to 81%) (Figure 4B). However, we selected clone 5.3 for further experiments as it expressed the highest level of pluripotency markers at the hESC stage and epicardial markers after directed differentiation both with and without tetracycline (Figures S3D and S3E). We then constructed 3D-EHTs combining CMs and sOPTiKD-FN1 EPI clone 5.3 and validated our approach, finding that FN1 deposition was decreased after tetracycline exposure of 3D-EHTs containing sOPTiKD-FN1 EPI (Figures 4D, 4E, and S3F). We found that this temporal loss of FN1 following tetracycline exposure abrogated the beneficial effects caused by EPI on CM maturation and structure, including sarcomere length and alignment (Figures 4F and 4G). Additionally, active force generation was reduced in 3D-EHTs containing sOPTiKD-FN1 EPI that were exposed to tetracycline (Figures 4H and 4I), while no effect was observed on passive force generation (Figures 4J and 4K). Furthermore, tetracycline-induced KD of FN1 resulted in increased time to peak fluorescence but had no significant impact on Ca^{2+} upstroke velocity or Ca^{2+} decay times (Figures 4L–4O).

Although these results continued to show that FN1 deposition in 3D-EHTs was a major component of the

(C–E) 3D-EHTs containing CM alone or EPI + CM, untreated or treated with pUR4. (C) Confocal images showing FN1 deposition following treatment with pUR4. Scale bar, 5 μm. (D) Quantification of FN1 following inhibition with pUR4. (E) Confocal images showing expression of integrin α5β1 following treatment with pUR4.

(F and G) Structural cardiac maturation as expressed by sarcomeric length (F) and sarcomere alignment (G) in 3D-EHTs containing CM only or CM + EPI with or without treatment with pUR4.

(H and I) Frank-Starling curves of active force generation (H) and slopes of active force (I) of 3D-EHTs containing CM only, CM + pUR4, CM + EPI, or CM + EPI + pUR4.

(J and K) Frank-Starling curves of passive force generation of 3D-EHTs containing CM only, CM + pUR4, CM + EPI, or CM + EPI + pUR4.

(L–O) Ca^{2+} kinetics of 3D-EHTs containing CM only or CM + EPI with or without treatment with pUR4. All experimental groups had N = 3 biological replicates. (L and M) Ca2+ kinetics including upstroke velocity and time to peak fluorescence of 3D-EHTs containing CM only or CM+EPI with or without treatment with pUR4. (N and O) Ca2+ kinetics including time to 50% decay and time to 90% decay of 3D-EHTs containing CM only or CM+EPI with or without treatment with pUR4. Mean values; error bars represent SEM. *p < 0.05, **p < 0.005, ***p < 0.001, ****p < 0.0001.

Please cite this article in press as: Ong et al., Epicardially secreted fibronectin drives cardiomyocyte maturation in 3D-engineered heart tissues, Stem Cell Reports (2023), https://doi.org/10.1016/j.stemcr.2023.03.002

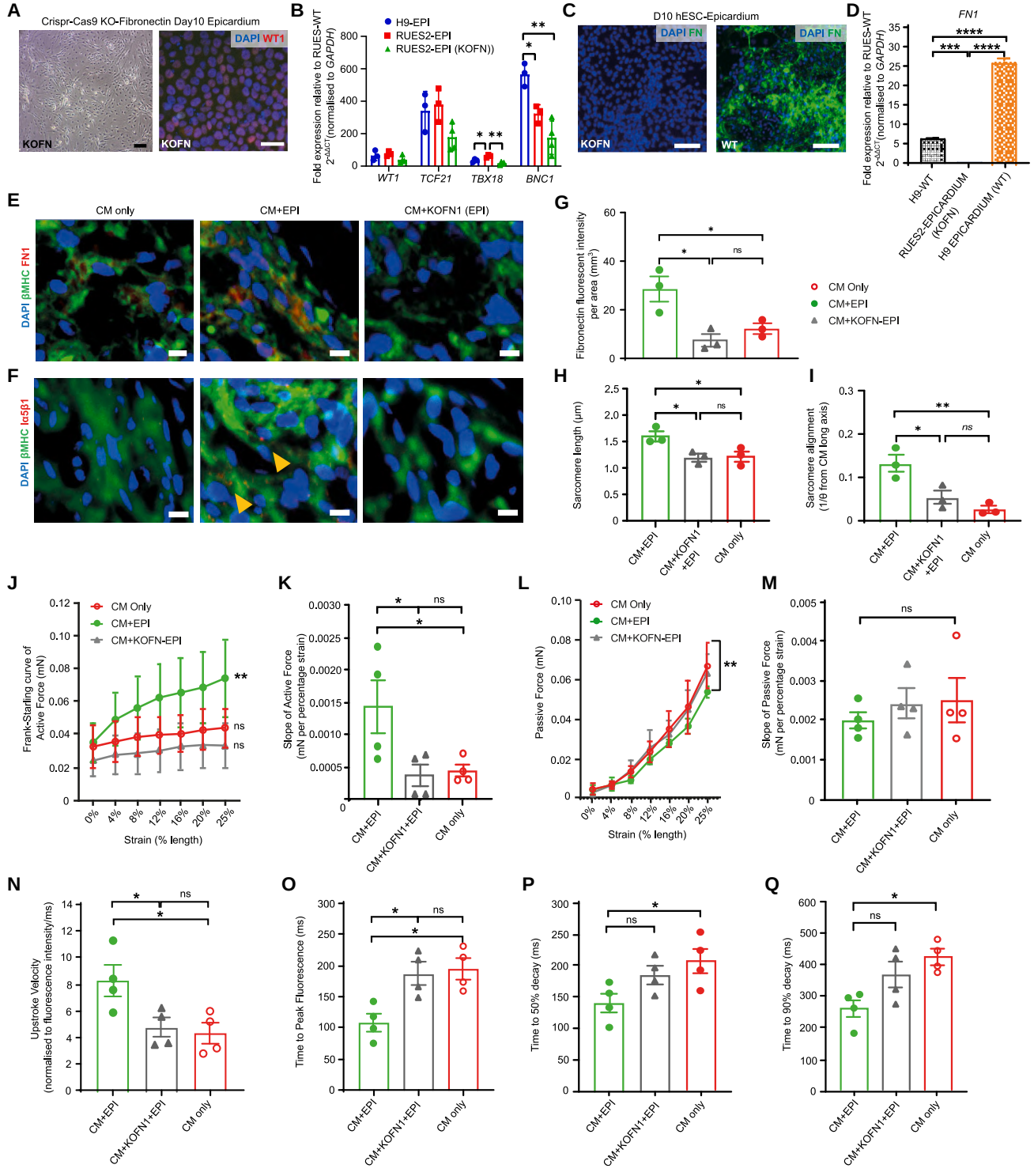

Figure 3. Constitutive loss of epicardial FN1 using a Crispr-Cas9-edited KO hESC line results in impaired CM maturation

(A) Cobblestone morphology and WT1 expression in Crispr-Cas9-edited KO FN1 epicardium. Scale bar, 20 μm.

(B) RNA expression of the key epicardial markers *WT1*, *TCF21*, *TBX18*, and *BNC1* in EPIs derived from H9-hESCs, RUES2-hESCs, and RUES2-hESC with KOFN.

(C) Confocal images showing FN1 expression in day 10 epicardium in KOFN and WT EPIs respectively. Scale bar, 50 μm.

(legend continued on next page)

epicardial effect, it was not clear if FN1 acts independently of other epicardial mechanisms. Therefore, finally we tested whether the addition of recombinant human FN1 (rhFN1) to CM-only 3D-EHTs could reproduce the effects elicited on CMs by hPSC-EPI in 3D-EHTs. We found that rhFN added to 3D-EHTs at concentrations of 10 μg/mL, 50 μg/mL, and 100 μg/m resulted in significant increases in sarcomeric length compared with untreated 3D-EHTs (Figures 5A and 5B). Moreover, improvements in sarcomere length were positively correlated with rhFN dose (one-tailed Pearson correlation; $p < 0.05$). We confirmed that FN1 was detectable in supplemented 3D-EHTs at greater levels than in 3D-EHTs without supplementation, but not at levels exceeding those seen in hESC-EPI-containing constructs (Figures 5C and 5D). Additionally, we found that 3D-EHTs treated with 100 μg/mL rhFN generated more active force than untreated 3D-EHTs, in line with hESC-EPI-containing constructs (Figures 5E and 5F). Furthermore, lower doses of rhFN also appeared to increase the passive force of 3D-EHTs (Figures 5G and 5H). However, the addition of rhFN to 3D-EHTs had no effect on Ca^{2+} handling (Figures 5I–5L).

Overall, these results provide further evidence that FN1 is required for the full positive effect of hESC-EPI on CM maturation. Moreover, by decoupling FN1 from epicardium, we have shown that FN1 may act independently to increase CM structure and function.

The EPI-CM interactome reveals a regulatory gene network driving cardiac development and regeneration

FN1 may only be one facet of EPI-CM crosstalk that regulates myocardial growth and maturation. Therefore, we investigated the interface of secreted epicardial factors and membrane-bound cell surface receptors on CMs and the role of FN1 within. To do so, we used bulk RNA-sequencing data from H9-derived hESC-EPI and hESC-CM to extract the EPI secretome and the CM membranome. A schematic of the experiment is shown in Figure 6A and the technical validation is depicted in Figure S5.

We first performed a differential expression analysis between the hESC-EPI and neural crest (NC), using DESeq2. As previously described, H9-hESC-NC was chosen as a negative control due to its redundancy in CM maturation and development (Bargehr et al., 2019). Significantly upregulated EPI genes were filtered to retain only genes encoding putatively secreted proteins according to the Human Protein Atlas (HPA) (http://www.proteinatlas.org/humanproteome/secretome) (Uhlén et al., 2019). This dataset is called the epicardial secretome (Figure 6B; Table S1). In parallel, differential expression analysis was performed between day 30 hESC-CM and H9-hESCs before differentiation. Significantly upregulated CM genes were filtered and restricted to genes encoding receptors and proteins with predicted membrane-anchored regions according to the HPA (Uhlén et al., 2019). This dataset is termed the CM membranome (Figure 6B; Table S1). In total, we found a potential secretome of 379 upregulated epicardial factors and a membranome of 1,417 upregulated CM receptors (Figure 6B; Table S1).

Next, to determine the EPI-CM interactome, these gene lists were connected, revealing a network of secreted epicardial factors and their respective membrane-bound receptors on CMs. We used the protein interaction database STRINGdb v11 (https://string-db.org/cgi/download.pl [2019 11 29]), which covered 99.5% and 95.5% of the upregulated secretome and membranome genes respectively. We constructed the interactome by filtering the secretome to retain genes that interacted with genes found only within the membranome. We then subset this list by only including interactions with a minimum experimental evidence score of above 400 for a higher confidence network (Figure 6C). Each interaction pair with a combined confidence score of above 700 was then functionally annotated following a manual literature review, categorizing the pathways where possible into the following regenerative roles: CM

(D) RNA expression of *FN1* in H9-WT, H9-EPI, and RUES2-EPI.
(E–Q) EPIs and CMs were derived from RUES2 hESC.
(E and F) Confocal images showing FN1 (E) and α5β1 expression (F) in 3D-EHTs of constructs containing CM only, CM + EPI, or CM + KOFN EPI. Scale bar, 5 μm.
(G) Quantification of FN1 expression by fluorescent intensity.
(H and I) Structural cardiac maturation as expressed by sarcomeric length (H) and sarcomere alignment (I) in 3D-EHTs containing CM only, CM + EPI, or CM + KOFN EPI.
(J and K) Frank-Starling curves of active force generation (J) and slopes of active force (K) of 3D-EHTs containing CM only, CM + EPI, or CM + KOFN EPI.
(L and M) Frank-Starling curves of passive force generation (L) and slopes of passive force (M) of 3D-EHTs containing CM only, CM + EPI, or CM + KOFN EPI.
(N–Q) Ca^{2+}-kinetics of 3D-EHTs containing CM only, CM + EPI, or KOFN EPI.
(E–Q) EPIs and CMs were derived from RUES2 hESC. All experimental groups had N = 4 biological replicates. Mean values; error bars represent SEM. *$p < 0.05$, **$p < 0.005$, ***$p < 0.001$, ****$p < 0.0001$. Two-sided p values were calculated using a one-way ANOVA with *post hoc* correction for multiple comparisons.

Please cite this article in press as: Ong et al., Epicardially secreted fibronectin drives cardiomyocyte maturation in 3D-engineered heart tissues, Stem Cell Reports (2023), https://doi.org/10.1016/j.stemcr.2023.03.002

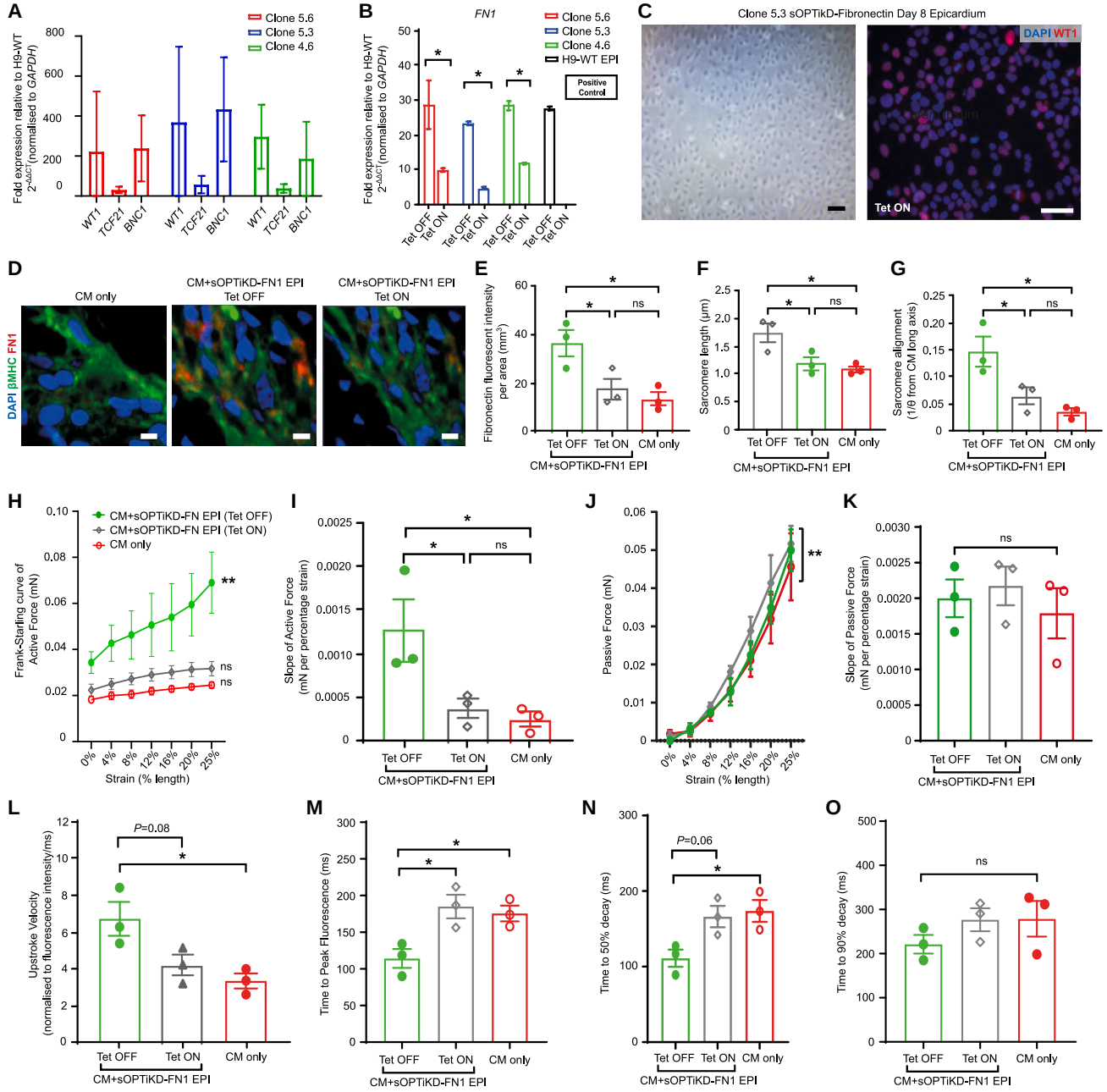

Figure 4. Temporal loss of epicardial FN1 expression with a tetracycline-inducible KD is sufficient to abrogate CM maturation

(A) RNA expression of the key epicardial markers *WT1*, *TCF21*, and *BNC1* in three sOPTiKD-FN1 clones, with the highest expression in clone 5.3.

(B) RNA expression in three sOPTiKD-FN1 clones following tetracycline exposure, with the greatest reduction in clone 5.3.

(C) Cobblestone morphology and WT1 expression in clone 5.3 differentiated to D8 hESC epicardium following 24 h of tetracycline induction. Scale bar, 20 μm.

(D) Confocal images showing FN1 expression in 3D-EHTs containing CM only, CM + sOPTiKD-FN1 EPI without tetracycline, and CM + sOPTiKD-FN1 EPI exposed to tetracycline.

(E) Quantification of FN1 expression by fluorescent intensity.

(F and G) Structural cardiac maturation as expressed by sarcomeric length (F) and sarcomere alignment (G) in 3D-EHTs containing CM only, CM + sOPTiKD-FN1 EPI without tetracycline, and CM + sOPTiKD-FN1 EPI exposed to tetracycline.

(H and I) Frank-Starling curves of active force generation (H) and slopes of active force (I) of 3D-EHTs containing CM only, CM + sOPTiKD-FN1 EPI without tetracycline, and CM + sOPTiKD-FN1 EPI exposed to tetracycline.

(legend continued on next page)

proliferation, maturation, survival, angiogenesis, development, extracellular matrix (ECM) regulation, inflammation, metabolism, and, more broadly, regeneration. Gene-pairs were then assigned to one or more of these roles (Table S1).

We found that FN1 was one component of a network of 23 predicted interactions between hESC-EPI and hESC-CM cells. Specifically, FN1 was predicted to interact in a proliferative role directly with integrins (subunits alpha 5 and beta 3) and c-MET via modulation of its ligand human growth factor, also secreted by hESC-EPI cells. Additionally, *FN1* appeared to interact with *EGFR* at the center of a hESC-CM membrane network targeted by an array of hESC-EPI factors with putative roles in ECM regulation, vasculogenesis, development, and survival among other regenerative functions (Figure 6C). Furthermore, we also predicted multiple *FN1* independent interactions between hESC-CM and hESC-EPI, including three from *RSPO1*, a recently identified regenerative epicardial protein (Li et al., 2019). Our EPI-CM interactome provides key insights into additional crosstalk between EPI and CM cells in our 3D-EHTs and presents a paracrine network that drives cardiac development and maturation in EHTs. Epicardial FN1 plays a genotypic and phenotypic key role in this process.

DISCUSSION

The addition of a stromal cell types such as the hESC-EPI to 3D-EHTs is seen to enhance hESC-CM contractile function and maturation (Bargehr et al., 2019). Although epicardial-myocardial crosstalk is likely responsible for this effect, the exact components or mechanisms governing the interaction remain unclear. Previous analysis on our 3D-EHTs placed FN1 as a likely candidate for further exploration as 3D-EHTs containing hESC-EPI had increased FN1 deposition and upregulated FN1 expression compared with hESC-NC (Bargehr et al., 2019). Here we confirm this hypothesis and provide several lines of evidence for an essential role of FN1 in improving CM maturation and function as part of the beneficial effect of hESC-EPIs as adjuvants in 3D-EHTs.

First, through histological analysis, we showed that the presence of epicardial FN1 was essential for maturation of the myofibril assembly. Without FN1, 3D-EHTs containing hESC-EPIs appeared histologically similar to those constructed with CMs alone. Second, by knocking out epicardial FN1 at both the gene and protein level, we consistently showed a loss of 3D-EHT function and CM maturity by observing a diminished active force-length relationship and inefficient excitation-contraction coupling, which are defining features of immature CMs (Karbassi et al., 2020). Moreover, this reduced functional performance was similar to 3D-EHTs constructed with hESC-CMs only, suggesting that, without FN1, the epicardium is unable to significantly improve upon these parameters and that FN1 is necessary for the full effect of hESC-EPI in driving hESC-CM maturation in collagen-based 3D-EHTs. We demonstrated that FN1-integrin binding was the key step in this process using pUR4. Third, we were able to recapitulate structural and functional benefits of adding hESC-EPI to 3D-EHTs by supplementing rhFN into CM-only constructs. However, unlike the addition of hESC-EPI cells to 3D-EHTs, we note that rhFN administered in this manner only increased the force of CM-only constructs and not Ca^{2+} handling. While these results demonstrate that FN1 is in itself capable of augmenting 3D-EHTs and that FN1 is necessary for the full epicardial effect, they also suggest that FN1 is not the only factor in mediating the beneficial interaction between hESC-EPIs and hESC-CMs.

We attempted to explore the additional interactions between hESC-EPI and hESC-CM cells within our 3D-EHTs using bioinformatics and found FN1 in a wider paracrine interactome between both cell types. Our interactome suggests that epicardial FN1 signals via a network of receptors and soluble factors to mediate the epicardial-myocardial crosstalk. In addition to CM maturation, further downstream functions were outlined, including ECM turnover, cell survival, proliferation, and angiogenesis. Experimentally assessing the contribution of epicardial FN1 toward these additional facets of cardiac regeneration was outside of the scope of this study as 3D-EHTs restricted our observations to maturation-based observations. Nonetheless, the interactome confirmed the necessary role of epicardial FN1 within EPI-CM crosstalk and revealed other signaling effectors that may drive CM maturation that require further exploration. This list of hESC-EPI-secreted factors provides a valuable resource of targets for insight into the mechanisms that govern CM maturation. Using the interactome as a starting point, we propose that, through individual or combined perturbation, future studies may drive CM maturation using commercially available cytokines, factor-expressing microbeads, targeted genetic manipulation of the parental line, or the use of hESC-EPIs themselves, as previously described (Bargehr

(J and K) Frank-Starling curves of passive force generation (J) and slopes of passive force (K) of 3D-EHTs containing CM only, CM + sOPTiKD-FN1 EPI without tetracycline, and CM + sOPTiKD-FN1 EPI exposed to tetracycline.
(L–O) Ca^{2+} kinetics of 3D-EHTs containing CM only, CM + sOPTiKD-FN1 EPI without tetracycline, and CM + sOPTiKD-FN1 EPI exposed to tetracycline. Each experimental group included N = 3 biological replicates. Mean values; error bars represent SEM. *p < 0.05, **p < 0.005. Two-sided p values were calculated using a one-way ANOVA with *post hoc* correction for multiple comparisons.

Please cite this article in press as: Ong et al., Epicardially secreted fibronectin drives cardiomyocyte maturation in 3D-engineered heart tissues, Stem Cell Reports (2023), https://doi.org/10.1016/j.stemcr.2023.03.002

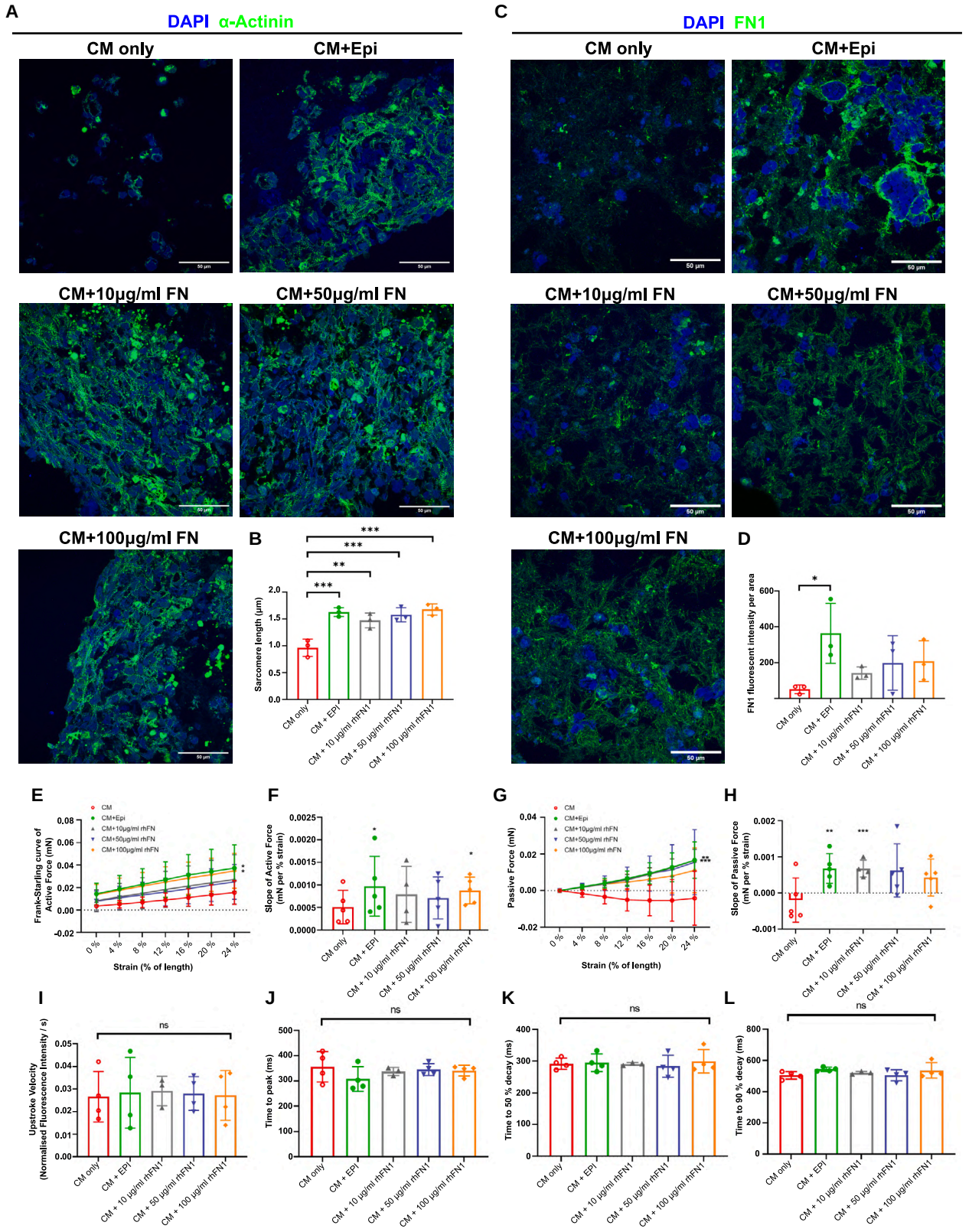

(legend on next page)

et al., 2019; Iyer et al., 2015). Collectively, this interactome provides the basis to understand the beneficial effects of hESC-EPIs on structure and function of hESC-CMs by elucidating the underlying mechanistic pathways. While the epicardium is a prominent example of a cell lineage that supports cardiac development and repair, we encourage the use of these data to guide investigations on other cell types to study their regenerative function, including cardiac fibroblasts, endothelial cells, and smooth muscle cells. Code describing the derivation of the interactome is openly accessible and can be used by other groups to investigate the interaction between diverse cell types (GitHub: https://github.com/Hindrance/EpiSciData2020).

We hypothesize that a loss of FN1 impairs hESC-CM maturation through a decrease of integrin-α5β1 clustering and downstream signaling as observed in this study. Normally, FN1 polymerization activates cell-surface integrin-α5β1 receptors (Wickström et al. 2011; Israeli-Rosenberg et al., 2014) as an interface between extracellular and intracellular communication. Active integrins act as mechano-transducers, converting environmental mechanical cues into biochemical signals (Israeli-Rosenberg et al., 2014) that govern the cellular responses such as cell migration, survival, cell cycle progression, and differentiation (Schwarzbauer and DeSimone 2011; Wickström et al. 2011). The FN1-integrin interaction in hESC-CMs may transmit these crucial biophysical and biochemical signals for communicating environmental cues, and subsequently regulate maturation and function. We propose that the loss of epicardial FN1 impairs the ability of hESC-CMs to respond to the environment by attenuating outside-inside signaling.

Despite the wide evolutionary distance, the phenotype induced in 3D-EHTs by loss of epicardial FN1 paralleled the observations within the zebrafish. In the injured zebrafish, activated EPIs secrete FN1, which binds to integrinβ3 receptors to recruit CMs within the site of injury (Wang et al., 2013). FN1 loss-of-function mutations disrupt zebrafish heart regeneration, leading to fibrosis instead of a contiguous wall of new muscle (Wang et al., 2013). We note that epicardial FN1 is highly expressed in zebrafish ECM, which may facilitate the ability of the zebrafish to successfully regenerate cardiac tissue (Mercer et al. 2013). While the dynamic nature of epicardial FN1 in human cellular models remains unclear, the role of epicardial FN1 in mediating epicardial-myocardial crosstalk to promote CM function appears to be conserved across species and broadens the relevance of our findings.

The applications for cardiac repair have grown exponentially over the past decade, ranging from direct intramyocardial injection of hPSC-derived cardiovascular cells to tissue engineering approaches and *in vitro* generation of complex tissues. While our study further highlights the complex nature of the mechanisms underlying these approaches, we have revealed one major interaction and a further network of mechanisms that may be used to optimize therapeutic approaches according to their application. For instance, tissue-engineered cardiovascular patches might prioritize the induction of vasculogenesis post transplantation over the regulation of ECM and inflammation post myocardial infarction (MI). Hence, one could selectively activate the angiogenic signaling pathways predicted by our interactome using individualized tissue constructs or microbeads that express activating factors. In contrast, for direct intramyocardial grafting of hESC-CMs, cells could be structurally and functionally matured *in vitro*, prior to transplantation targeting anti-inflammatory and pro-survival alongside ECM regulation pathways to dictate therapeutic success. Alternatively, for *in vitro* applications such as drug toxicity assays (for example, assays using chemotherapeutics to elicit toxic effects and arrhythmias), one may focus on activating cardiac maturation pathways to generate CMs with a more robust readout, more closely resembling the drug response exhibited by patients.

There were limitations within this study. Namely, experiments were carried out on small sample sizes, and biological variability was seen across all replicates when assessing force generation, Ca^{2+} handling, and sarcomeric assembly. We attribute this variability to independent cellular differentiations despite the use of robust differentiation

Figure 5. The addition of rhFN1 increases hPSC-CM maturity in 3D-EHTs without the presence of hPSC-EPI

(A) Immunofluorescent imaging of 3D-EHTs shows the arrangement of alpha-actinin within sarcomeres and localization of connexin-43 in constructs containing hPSC-CMs, hPSC-CMs + hPSC-EPIs, or hPSC-CMs + rhFN1 at varied concentrations; sarcomere lengths are quantified in (B). (C) Immunofluorescent imaging of 3D-EHTs highlighting the quantify of FN1 and collagen deposited within constructs containing hPSC-CMs, hPSC-CMs + hPSC-EPIs, or hPSC-CMs + rhFN1 at varied concentrations; FN1 intensities are quantified in (D).

(E–H) (E) Frank-Starling curves of active force generation and (F) slopes of active force, as well as (G) curves of passive force and (H) slopes of passive force measured from 3D-EHTs containing hPSC-CMs, hPSC-CMs + hPSC-EPIs, or hPSC-CMs + rhFN1 at varied concentrations.

(I–L) Ca^{2+} kinetics of 3D-EHTs containing hPSC-CMs, hPSC-CMs + hPSC-EPIs, or hPSC-CMs + rhFN1 at varied concentrations. Each experimental group included a minimum of N = 3 biological replicates. (I and J) Ca^{2+} kinetics including upstroke velocity and time to peak fluorescence of 3D-EHTs containing hPSC-CMs, hPSC-CMs + hPSC-EPIs, or hPSC-CMs + rhFN1 at varied concentrations. (K and L) Ca2+ kinetics including time to 50% decay and time to 90% decay of 3D-EHTs containing hPSC-CMs, hPSC-CMs + hPSC-EPIs, or hPSC-CMs + rhFN1 at varied concentrations. Mean values; error bars represent SEM. *$p < 0.05$, **$p < 0.005$.

Please cite this article in press as: Ong et al., Epicardially secreted fibronectin drives cardiomyocyte maturation in 3D-engineered heart tissues, Stem Cell Reports (2023), https://doi.org/10.1016/j.stemcr.2023.03.002

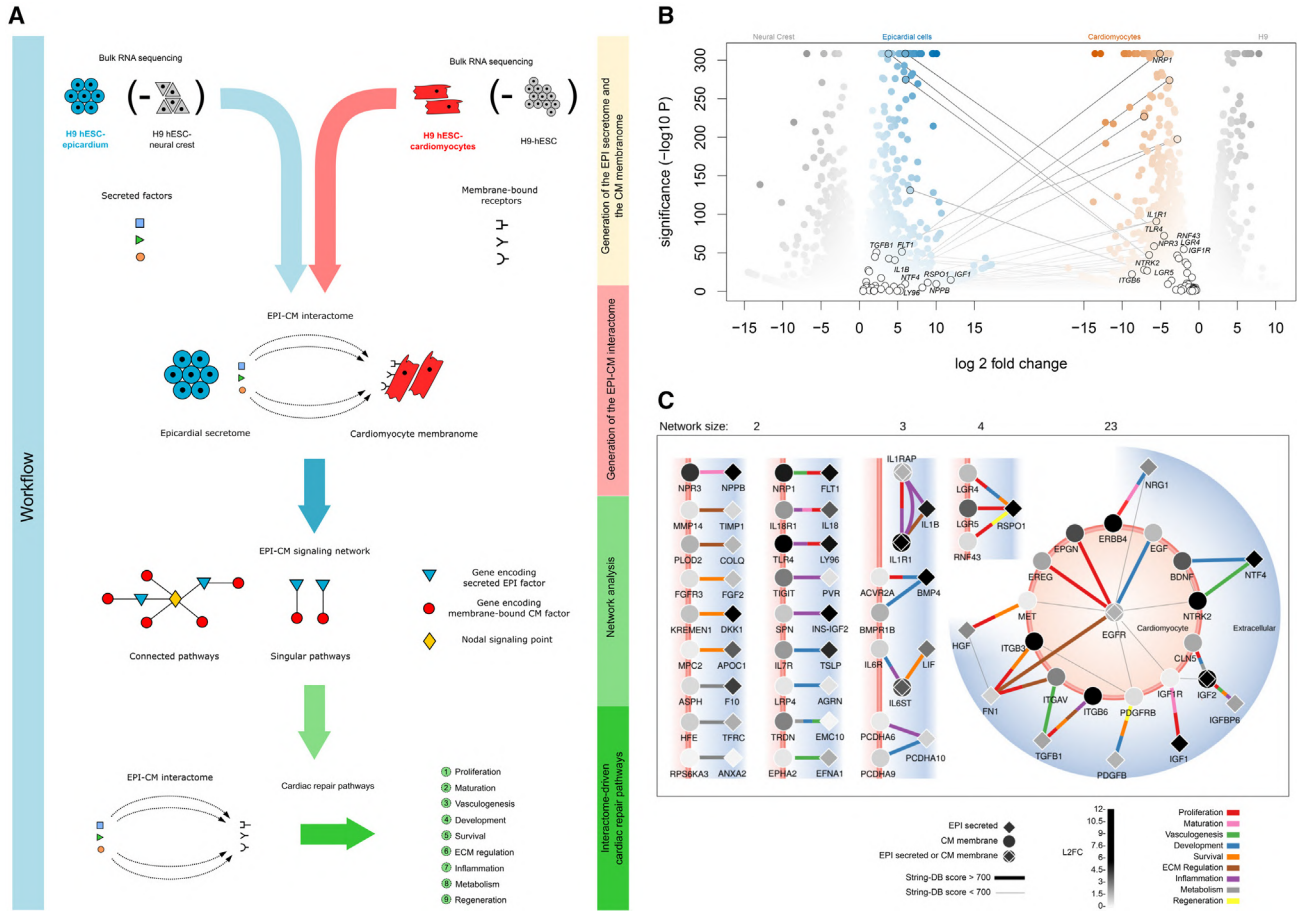

Figure 6. The EPI-CM interactome reveals a regulatory gene network driving cardiac development and regeneration

(A) Schematic overview of the study design and experimental procedure. Epicardial secretome and CM membranome were first derived using RNA sequencing. Both datasets were next integrated to generate the EPI-CM interactome, revealing a unique signaling network of regenerative pathways driving cardiac development and tissue repair. All pathways were finally ascribed reparative categories constituting a reference library for cardiac repair.

(B) The interactome between hESC-EPI secretome and hESC-CM membranome. Blue nodes on the left represent genes encoding for secreted factors expressed by hESC-EPIs compared with expression in hESC-NC, shown in gray. Orange nodes on the right depict genes encoding membrane-bound receptors expressed by hESC-CM compared with hESC. All binary hESC-EPI to hESC-CM interactions with an experimental score of above 700 in STRINGdb are shown, including a second layer of interactions formed from associations with an experimental score above 400. Respective interactions are shown with gray lines. CEPI-CM regulatory gene network driving cardiac development and regeneration.

(C) hESC-EPI-secreted genes are shown as diamond symbols on blue background, and hESC-CM membrane genes are displayed as circles on red background. Interactions with a STRINGdb score of greater than 700 are shown as bold lines and those with a STRINGdb score of less than 700 as fine lines. Strength of gene expression is expressed as L2FC and visualized by the gray tone in hESC-EPI-secreted and hESC-CM membrane gene symbols. The color of the connecting line between two genes describes the reparative category based on a manual literature review with references cited in Table S1. hESC, human embryonic stem cell; hESC-EPI, human embryonic stem cell-derived EPIs; hESC-CM, human embryonic stem cell-derived CMs; hESC-NC, human embryonic stem cell-derived neural crest cells.

protocols (Iyer et al., 2015; Bargehr et al., 2019). In particular, this affected our assessment of Ca^{2+} handling using fluorescent trace analysis as it is less sensitive than the assessment of force generation on a myograph. However, while individual Ca^{2+}-handling experiments were unable to show effect size clearly, we increased statistical power by pooling the data of experiments shown in (Figures 1, 2, and 3) and demonstrated significant differences in all Ca^{2+}-handling parameters between CM 3D-EHTs generated with or without hESC-EPI. Nonetheless, 3D-EHTs are the most physiologically relevant model to assess hESC-CM maturation as they enable functional readouts such as

active force-length relationship and Ca^{2+} handling (Karbassi et al., 2020). These limitations were addressed prior to experiments by ensuring that hESC-CM differentiations were pure (>80% positive for cardiac troponin T [cTNT]), and that cell viability was optimized using with a 42°C heat shock prior to constructing the 3D-EHTs. Furthermore, our hESC-EPI dose optimization experiments were performed only using hESC-EPIs derived from the H9 cell line. Although we have previously shown the benefits of hESC-EPIs on 3D-EHTs regardless of cell line (Bargehr et al., 2019), we admit that modest cell-line-dependent differences might exist at different hESC-EPI fractions. As such, the dose-response curves generated to optimize hESC-EPI content could be taken in the context of the cell line used and assessed during subsequent experiments. A final limitation is noted in the RNA-sequencing experiment that was performed on hESC derivatives *in vitro* and not from 3D-EHTs before or following transplantation. This analysis was not designed to draw conclusion about either the crosstalk between hESC-EPIs and hESC-CMs following transplantation *in vivo* or the crosstalk between primary EPIs and CMs.

To conclude, we demonstrated that FN1 promotes hESC-CM maturation and function in 3D-EHTs across a series of FN1 loss-of-function experiments and a gain-of-function experiment. Our findings implied that a loss of FN1 reduced integrin clustering and therefore signaling with hESC-CMs directed by the epicardium and epicardial FN1. Considering these results, we conclude that epicardial FN1 is necessary for mediating the full effect of hESC-EPIs in driving CM maturation in 3D-EHTs. Our epicardial-myocardial interactome expands on this key observation and highlights other components of epicardial-myocardial crosstalk that regulate proliferation, survival, angiogenesis, and ECM turnover, all processes crucial to achieving robust cardiac regeneration. Last, we conclude that our new understanding of FN1 and additional interactome may guide the development of individualized next-generation cardiac tissues for heart regeneration.

EXPERIMENTAL PROCEDURES

Resource availability

Corresponding authors

Dr. Lay Ping Ong (lpo20@cam.ac.uk) or Professor Sanjay Sinha (ss661@cam.ac.uk).

Materials availability

hESC lines used for this project are available from the corresponding authors with a completed materials transfer agreement.

Data and code availability

Data supporting the findings of this study are available within the main and supplemental manuscript. RNA-sequencing experiments are available from published datasets previously deposited in the NCBI's Gene Expression Omnibus under accession number GSE122714 for hESC-EPI and hESC-NC and GSE85331 for the hESC-CM (Liu et al., 2017) and hESC-EPI (Bargehr et al., 2019). Code generated to produce the interactome is available online (GitHub https://github.com/Hindrance/EpiSciData2020).

Differentiation of hESC-CM and hESC-EPI

EPIs were differentiated from H9 hESCs (WiCell, Madison) and from RUES2 (female line, Rockefeller University, NIH registry number 0013), respectively. The differentiation protocol was as previously described (Iyer et al., 2016). To differentiate into epicardium, cells were singly suspended in CDM-PVA, WNT3A (25 ng/mL, R&D), BMP4 (50 ng/mL), and retinoic acid (4 μM, Sigma) at a seeding density of 2.5×10^4 cells/cm^2 and replated for exactly 10 days with medium change every 5 days. CMs were differentiated from RUES2 cells as previously described (Bargehr et al., 2019) using the ABCX method (see supplemental experimental procedures). Respective karyotypes are shown in Figure S6.

Generation and characterization of 3D-EHTs

3D-EHTs were constructed in polydimethylsiloxane (PDMS) (PDMS, Sylgard 184; Dow Corning, Midland, MI) wells by combining hESC-CM and hESC-EPI in a collagen-based hydrogel as previously described (Bargehr et al., 2019).

To conduct Frank-Starling force measurements, 3D-EHTs were removed from the PDMS wells and suspended between a force transducer (Aurora Scientific, model 400A) and length controller (Aurora Scientific, model 312B). Both passive tension and active force traces were recorded and analyzed using customized LabView and MATLAB software. For non-ratiometric assessment of Ca^{2+} handling, 3D-EHTs were incubated with Fluo-4 AM (Molecular Probes, Invitrogen). Then, videos were recorded at both intrinsic contractile rates and paced at 1, 1.5, and 2 Hz before being analyzed with customized MATLAB software. Final analysis made use of Ca^{2+} data from constructs paced at 1 Hz. Representative force and Ca^{2+} traces are depicted in Figure S4. 3D-EHTs were subsequently cryo-embedded and sectioned on a cryotome prior to IHC and quantitative assessment of morphological endpoints.

Loss of function of epicardial FN

Pharmacological inhibition of epicardial FN1 with pUR4 (Genescript) was performed on day 7 of epicardial differentiation at a concentration of 500 nm for 72 h. Furthermore, 10 μL of pUR4 (500 nM) were included in the gel mixture during 3D-EHTs generation and along with medium, changed on alternate days over 14 days. FN, the protein, was subsequently quantified by western blot. The western blot technique is described in detail within supplemental experimental procedures.

To generate CRISPR-Cas9-mediated KO FN (KOFN1) hESC line, an FN1-targeted sgRNA was chosen from Genscript (https://www.genscript.com/gRNA-database.html), and cloned in pX459 (Addgene #62988 all according to a Zhang lab protocol (https://www.addgene.org/crispr/zhang/PX459-SpCas9+sgRNA). The sgRNA sequence was (5′ to 3′) CACCGTACAAACCAACGCATTGCCT with (3′ to 5′) CATGTTTGGTTGCGTAACGGACAAA. Gene targeting was done via gene juice-mediated transfection and with subsequent

genotyping of the targeted clones, as further described in the supplemental experimental procedures.

For generation of an inducible FN KD (sOPTiKD-FN1) hESC line, a short hairpin RNA (shRNA) was selected from the Broad Institute TRC library (Moffat et al., 2006). The shRNA sequences for psOPTIkd vector construction were as follows: top (5′ to 3′) GATCCCGCCTGCTCCAAGAATTGGTTTCTCGAGAAACCAATTCTTGGAGCAGGCTTTTYTG and bottom (5′ to 3′) TCGACAAAAAAGCCTGCTCCAAGAATTGGTTTCTCGAGAAACCAATTCTTGGAGCAGGCGG. BglII overhang is in red, and terminator sequence/SalI overhang in blue.

The shRNA was into pAAV-Puro_siKD (a gift from the Vallier Group, University of Cambridge; Addgene #86695) as previously described (Bertero et al., 2016). Gene targeting was done via gene juice-mediated transfection and is described in detail in the supplemental experimental procedures along with the genotyping of the targeted clones. Differentiation of hESC epicardium was carried out in the absence of tetracycline. Tetracycline was added 2 days prior to harvest, after epicardial differentiation and maintained when 3D-EHTs were generated.

Recombinant human FN1 dose-response assay

Human plasma FN (rhFN) (Merck, F2006) was integrated into the tissue constructs at concentrations of 10, 50, and 100 μg/mL of the total tissue construct volume through subtraction of the additional sterile water volume to compensate for the volume of supplemented rhFN. After reconstitution of the cells within the gel, the tissue suspension was cast into the PDMS molds and left to solidify in the incubator at 37°C for 30 min prior to being immersed in RPMI medium supplemented with B-27 (Gibco) and insulin. The 3D-EHTs were maintained with medium changes every 2 days prior to use. Spontaneous contractions were observed within 3 days.

Bulk RNA sequencing

Starting material for RNA sequencing was composed of H9 hESC-EPI, H9 hESC-NC, and H9 hESC-CM as well as undifferentiated H9 hESCs. The datasets had previously been deposited in the NCBI's Gene Expression Omnibus under accession number GSE122714 for hESC-EPI and hESC-NC and GSE85331 for the hESC-CM (Liu et al., 2017) and hESC-EPI (Bargehr et al., 2019).

Analysis of epicardial-CM interactome

We first performed a differential expression analysis between the hESC-EPI and hESC-NC, using DESeq2. As previously described, hESC-NCs were chosen as a negative control due to their redundancy in hESC-CM maturation and development. The list of differentially upregulated genes was filtered to retain only genes encoding putatively secreted proteins according to the HPA (http://www.proteinatlas.org/humanproteome/secretome) (Uhlén et al., 2019). This dataset is called the hESC-EPI secretome. In parallel, differential expression analysis was performed between day 30 hESC-CM and H9s before differentiation. The list of differentially expressed genes was filtered and restricted to genes encoding receptors and proteins with predicted membrane-anchored regions according to the HPA (Uhlén et al., 2019). This dataset is termed the hESC-CM membranome. Next, to determine the interactome, both gene lists were jointly analyzed to elucidate hESC-EPI-secreted factors and their respective membrane-bound receptors on hESC-CMs. We used the interaction database STRINGdb v11 (https://string-db.org/cgi/download.pl [2019 11 29]), which covered 99.5% and 95.5% of the upregulated secretome and membranome genes respectively. We constructed the interactome by filtering the secretome to retain genes with interactions with genes only found in the membranome. The interactome network is shown in Figure 6 and Table S1. The technical validation of the sequenced data and EPI/CM differentiation is detailed in the supplemental experimental procedures and Figure S5, respectively.

Statistical analysis

All *in vitro* studies were performed as three parallel technical replicates for each individual biological replicate. Each biological replicate was an independent experiment with EHTs generated on different days and measured separately, from different cellular differentiations. Statistical testing was only performed on biological replicates, using an unpaired t test for two-group comparisons and a paired t test for comparison of two paired groups. One-way ANOVA was used for the statistical comparison of more than two groups, and a *post hoc* Tukey test was used if the group variance was equal. As for groups with unequal variance, a *post hoc* Kruskal-Wallis test with Dunn's correction for multiple comparisons was applied. Measuring two-sided significance, a p value of 0.05 was considered statistically significant. All results are presented as mean ± SEM unless otherwise stated. All analyses were performed using GraphPad Prism 9.0 software.

SUPPLEMENTAL INFORMATION

Supplemental information can be found online at https://doi.org/10.1016/j.stemcr.2023.03.002.

AUTHOR CONTRIBUTIONS

L.P.O. designed the study, conducted the *in vitro* experiments, wrote the main manuscript, and prepared figures and tables. J.B. designed the bioinformatics study, and prepared figures and tables. V.R.K.-S. carried out the bioinformatics analysis, and prepared the figures and manuscript. J.L. conducted *in vitro* experiments, performed data analyses, and prepared figures. S.B. assisted in the analyses of the *in vitro* experiments. M.C. contributed to conceptual ideas and revised the manuscript. A.B., W.G.B., and S.M. advised on the generation of genetically edited hESC-KO and sOPTiKD cell lines and revised the manuscript. S.S. and L.G. designed the study, obtained research funding, edited, and approved the final version of the manuscript.

ACKNOWLEDGMENTS

This work was supported by the British Heart Foundation Oxbridge Centre for Regenerative Medicine RM/13/3/30159, RM/17/2/33380 and a BHF Senior Fellowship FS/18/46/33663 (L.G. and S.S.). S.S. was also supported by the British Heart Foundation Centre for Cardiovascular Research Excellence. L.P.O. is funded by a Wellcome Trust Fellowship (grant no. 203568/Z/16/Z). V.R.K.-S. and M.C. are supported by CRM (RM/17/2/33380). M.C. has also received support from BHF grant SP/15/7/31561.

We also acknowledge core support from the Wellcome Trust (203151/Z/16/Z) and the UKRI Medical Research Council (MC_PC_17230). For the purpose of open access, the author has applied a CC BY public copyright license to any Author Accepted Manuscript version arising from this submission.

CONFLICT OF INTERESTS

S.S. and J.B. are co-founders and shareholders in ABS Biotechnologies GmbH.

Received: February 7, 2022
Revised: February 28, 2023
Accepted: March 1, 2023
Published: March 30, 2023

REFERENCES

Astrof, S., Denise, C., and Hynes, R.O. (2007). Multiple cardiovascular defects caused by the absence of alternatively spliced segments of fibronectin. Dev. Bio. *311*, 11–24. https://doi.org/10.1016/j.ydbio.2007.07.005.

Bargehr, J., Ong, L.P., Colzani, M., Davaapil, H., Hofsteen, P., Bhandari, S., Gambardella, L., Le Novère, N., Iyer, D., Sampaziotis, F., et al. (2019). Epicardial cells derived from human embryonic stem cells augment cardiomyocyte-driven heart regeneration. Nat. Biotechnol. *37*, 895–906. https://doi.org/10.1038/s41587-019-0197-9.

Bertero, A., Pawlowski, M., Ortmann, D., Snijders, K., Yiangou, L., Cardoso De Brito, M., Brown, S., Bernard, W.G., Cooper, J.D., Giacomelli, E., et al. (2016). Optimized inducible ShRNA and CRISPR/Cas9 platforms for in vitro studies of human development using HPSCs. Development *143*, 4405–4418. https://doi.org/10.1242/dev.138081.

Bertero, A., Yiangou, L., Brown, S., Ortmann, D., Pawlowski, M., and Vallier, L. (2018). Conditional manipulation of gene function in human cells with optimized inducible ShRNA. Current Protocols in Stem Cell Biology *44*, 5C.4.1–5C.4.48. https://doi.org/10.1002/cpsc.45.

Chong, J.J.H., Yang, X., Don, C.W., Minami, E., Liu, Y.-W., Weyers, J.J., Mahoney, W.M., Van Biber, B., Cook, S.M., Palpant, N.J., et al. (2014). Human embryonic stem cell-derived cardiomyocytes regenerate non-human primate hearts. Nature *510*, 273–277. https://doi.org/10.1038/nature13233.Human.

Gittenberger-de Groot, A.C., Vrancken Peeters, M.P., Mentink, M.M., Gourdie, R.G., and Poelmann, R.E. (1998). Epicardium-derived cells contribute a novel population to the myocardial wall and the atrioventricular cushions. Circ. Res. *82*, 1043–1052. https://doi.org/10.1161/01.RES.82.10.1043.

Guadix, J.A., Carmona, R., Muñoz-Chápuli, R., and Pérez-Pomares, J.M. (2006). In vivo and in vitro analysis of the vasculogenic potential of avian proepicardial and epicardial cells. Dev. Dyn. *235*, 1014–1026. https://doi.org/10.1002/dvdy.20685.

Ieda, M., Tsuchihashi, T., Ivey, K.N., Ross, R.S., Hong, T.T., Shaw, R.M., and Srivastava, D. (2009). Cardiac fibroblasts regulate myocardial proliferation through B1 integrin signaling. Dev. Cell *16*, 233–244. https://doi.org/10.1016/j.devcel.2008.12.007.

Israeli-Rosenberg, S., Manso, A.M., Okada, H., and Ross, R.S. (2014). Integrins and integrin-associated proteins in the cardiac myocyte. Circ. Res. *114*, 572–586. https://doi.org/10.1161/CIRCRESAHA.114.301275.

Iyer, D., Gambardella, L., Bernard, W.G., et al. (2016). Robust derivation of epicardium and its differentiated smooth muscle cell progeny from human pluripotent stem cells. Development *143*, 904.

Iyer, D., Gambardella, L., Bernard, W.G., Serrano, F., Mascetti, V.L., Pedersen, R.A., Talasila, A., and Sinha, S. (2015). Robust derivation of epicardium and its differentiated smooth muscle cell progeny from human pluripotent stem cells. DevelopmentEngland *142*, 1528–1541. https://doi.org/10.1242/dev.119271.

Karbassi, E., Fenix, A., Marchiano, S., Muraoka, N., Nakamura, K., Yang, X., and Murry, C.E. (2020). Cardiomyocyte maturation: advances in knowledge and implications for regenerative medicine. Nat. Rev. Cardiol. *17*, 341–359. https://doi.org/10.1038/s41569-019-0331-x.

Knight-Schrijver, V.R., Davaapil, H., Bayraktar, S., Ross, A.D.B., Kanemaru, K., Cranley, J., Dabrowska, M., et al. (2022). A single-cell comparison of adult and fetal human epicardium defines the age-associated changes in epicardial activity. Nature Cardiovascular Research *1*, 1215–1229. https://doi.org/10.1038/s44161-022-00183-w.

Laflamme, M.A., Chen, K.Y., Naumova, A.V., Muskheli, V., Fugate, J.A., Dupras, S.K., Reinecke, H., Xu, C., Hassanipour, M., Police, S., et al. (2007). Cardiomyocytes derived from human embryonic stem cells in pro-survival factors enhance function of infarcted rat hearts. Nat. Biotechnol. *25*, 1015–1024. https://doi.org/10.1038/nbt1327.

Li, G., Tian, L., Goodyer, W., Kort, E.J., Buikema, J.W., Xu, A., Wu, J.C., Jovinge, S., and Wu, S.M. (2019). Single cell expression analysis reveals anatomical and cell cycle-dependent transcriptional shifts during heart development. Development *146*, dev173476.

Liu, Y.W., Chen, B., Yang, X., Fugate, J.A., Kalucki, F.A., Futakuchi-Tsuchida, A., Couture, L., Vogel, K.W., Astley, C.A., Baldessari, A., et al. (2018). Human embryonic stem cell-derived cardiomyocytes restore function in infarcted hearts of non-human primates. Nat. Biotechnol. *36*, 597–605. https://doi.org/10.1038/nbt.4162.

Liu, Q., Jiang, C., Xu, J., Zhao, M.T., Van Bortle, K., Cheng, X., et al. (2017). Genome-wide temporal profiling of transcriptome and open chromatin of early cardiomyocyte differentiation derived from hiPSCs and hESCs. Circ. Res. *121*, 376–391.

Mercer, S.E., Odelberg, S.J., and Simon, H.G. (2013). A dynamic spatiotemporal extracellular matrix facilitates epicardial-mediated vertebrate heart regeneration. Dev. Biol. *382*, 457–469. https://doi.org/10.1016/j.ydbio.2013.08.002.

Mittal, A., Pulina, M., Hou, S.Y., and Astrof, S. (2010). Fibronectin and integrin alpha 5 play essential roles in the development of the cardiac neural crest. Mech. Dev. *127*, 472–484. https://doi.org/10.1016/j.mod.2010.08.005.

Moffat, J., Grueneberg, D.A., Yang, X., et al. (2006). A lentiviral RNAi library for human and mouse genes applied to an arrayed viral high-content screen. Cell *124*, 1283–1298.

Schwarzbauer, J.E., and DeSimone, D.W. (2011). Fibronectins, their fibrillogenesis, and in vivo functions. Cold Spring Harb. Perspect. Biol. *3*, a005041. https://doi.org/10.1101/cshperspect.a005041.

Shiba, Y., Fernandes, S., Zhu, W.-zhong, Filice, D., Muskheli, V., Kim, J., Palpant, N.J., Gantz, J., Moyes, K.W., Reinecke, H., et al. (2013). HESC-derived cardiomyocytes electrically couple and suppress arrhythmias in injured hearts. Nature *489*, 322–325. https://doi.org/10.1038/nature11317.hESC-Derived.

Shiba, Y., Gomibuchi, T., Seto, T., Wada, Y., Ichimura, H., Tanaka, Y., Ogasawara, T., Okada, K., Shiba, N., Sakamoto, K., et al. (2016). Allogeneic transplantation of IPS cell-derived cardiomyocytes regenerates primate hearts. Nature *538*, 388–391. https://doi.org/10.1038/nature19815.

Tiburcy, M., Hudson, J.E., Balfanz, P., Schlick, S., Meyer, T., Chang Liao, M.L., Levent, E., Raad, F., Zeidler, S., Wingender, E., et al. (2017). Defined Engineered Human Myocardium with Advanced Maturation for Applications in Heart Failure Modelling and Repair. Circulation *135*, 1832–1847. https://doi.org/10.1161/CIRCULATIONAHA.116.024145.

Uhlén, M., Karlsson, M.J., Hober, A., Svensson, A.-S., Scheffel, J., Kotol, D., Zhong, W., et al. (2019). The Human Secretome. Science Signaling *12*, eaaz0274. https://doi.org/10.1126/scisignal.aaz0274.

Wang, J., Karra, R., Dickson, A.L., and Poss, K.D. (2013). Fibronectin is deposited by injury-activated epicardial cells and is necessary for zebrafish heart regeneration. Dev. Biol. *382*, 427–435. https://doi.org/10.1016/j.ydbio.2013.08.012.

Weinberger, F., Breckwoldt, K., Pecha, S., Kelly, A., Geertz, B., Starbatty, J., Yorgan, T., Cheng, K.H., Lessmann, K., Stolen, T., et al. (2016). Cardiac repair in Guinea pigs with human engineered heart tissue from induced pluripotent stem cells. Sci. Transl. Med. *8*, 363ra148. https://doi.org/10.1126/scitranslmed.aaf8781.

Wickström, S.A., Radovanac, K., and Fässler, R. (2011). Genetic analyses of integrin signaling. Cold Spring Harb. Perspect. Biol. *3*, a005116. https://doi.org/10.1101/cshperspect.a005116.

Zarrinkoub, R., Wettermark, B., Wändell, P., Mejhert, M., Szulkin, R., Ljunggren, G., and Kahan, T. (2013). The epidemiology of heart failure, based on data for 2.1 million inhabitants in Sweden. Eur. J. Heart Fail. *15*, 995–1002. https://doi.org/10.1093/eurjhf/hft064.

Ziaeian, B., and Fonarow, G.C. (2016). Epidemiology and aetiology of heart failure. Nat. Rev. Cardiol. *13*, 368–378. https://doi.org/10.1038/nrcardio.2016.25.

Stem Cell Reports, Volume *18*

Supplemental Information

Epicardially secreted fibronectin drives cardiomyocyte maturation in 3D-engineered heart tissues

Lay Ping Ong, Johannes Bargehr, Vincent R. Knight-Schrijver, Jonathan Lee, Maria Colzani, Semih Bayraktar, William G. Bernard, Silvia Marchiano, Alessandro Bertero, Charles E. Murry, Laure Gambardella, and Sanjay Sinha

Supplementary Information

Epicardially-secreted Fibronectin drives cardiomyocyte maturation in 3D-engineered heart tissues.

Lay Ping Ong[1,2*], Johannes Bargehr[1,2*], Vincent R. Knight-Schrijver[1,2*], Jonathan Lee[1,2], Maria Colzani[1,2], Semih Bayraktar[1,2], William G. Bernard[1,2], Silvia Marchiano[3], Alessandro Bertero[4], Charles E. Murry[3], Laure Gambardella[1,2Ω] and Sanjay Sinha[1,2Ω]

1. Wellcome – MRC Cambridge Stem Cell Institute, Jeffrey Cheah Biomedical Centre, Cambridge Biomedical Campus, University of Cambridge, Puddicombe Way, CB2 0AW Cambridge, UK
2. Division of Cardiovascular Medicine, University of Cambridge, ACCI Level 6, Box 110, Addenbrooke's Hospital, Hills Road, Cambridge CB2 0QQ, UK
3. Departments of Laboratory Medicine & Pathology, Bioengineering, and Medicine/Cardiology; Center for Cardiovascular Biology, Institute for Stem Cell and Regenerative Medicine, University of Washington, Seattle, WA, USA.
4. Molecular Biotechnology Center, Department of Molecular Biotechnology and Health Sciences, University of Torino, Via Nizza 52, 10126 Torino, Italy.

Supplementary Figure 1. Passive force and Ca^{2+}-kinetics of 3D-EHTs with optimised cell ratios.

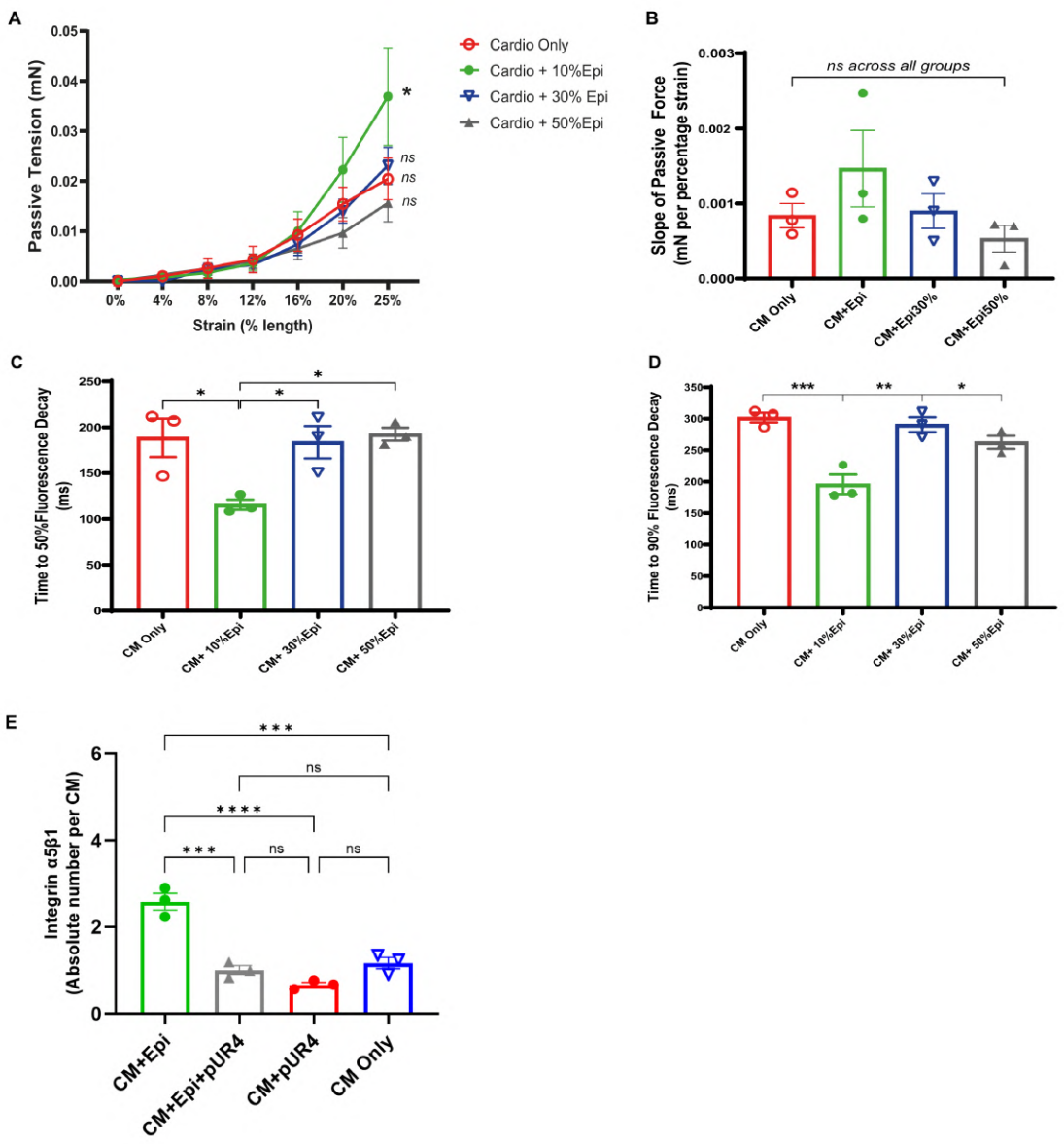

Supp Figure 1. Passive force and Ca^{2+}-kinetics of 3D-EHTs with optimised cell ratios. (A) Frank-Starling curves of passive force generation of 3D-EHTs containing CM only, CM+10% hESC-epicardium, CM+30% hESC-epicardium or CM+50% hESC-epicardium. **(B)** Slope of active force generation. **(C-D)** Ca^{2+}-upstroke velocity **(C)** and time to 90% fluorescence decay **(D)** of 3D-EHTs containing CM only, CM+10% hESC-epicardium, CM+30% hESC-epicardium or CM+50% hESC-epicardium. **(E)** Quantification of Integrin α5β1 in 3D-EHTs containing, CM+EPI, CM+EPI+PUR4, CM+PUR4 or CM only. Mean values; error bars represent s.e.m. **P*<0.05. ** *P*<0.005 *** *P*<0.0001. Two-sided *P* values were calculated using a one-way ANOVA with post-hoc correction for multiple comparisons. Each experimental group included *N*=3 biological replicates.

Supplementary Figure 2: Generation of Crispr-Cas9 Knockout FN cell line.

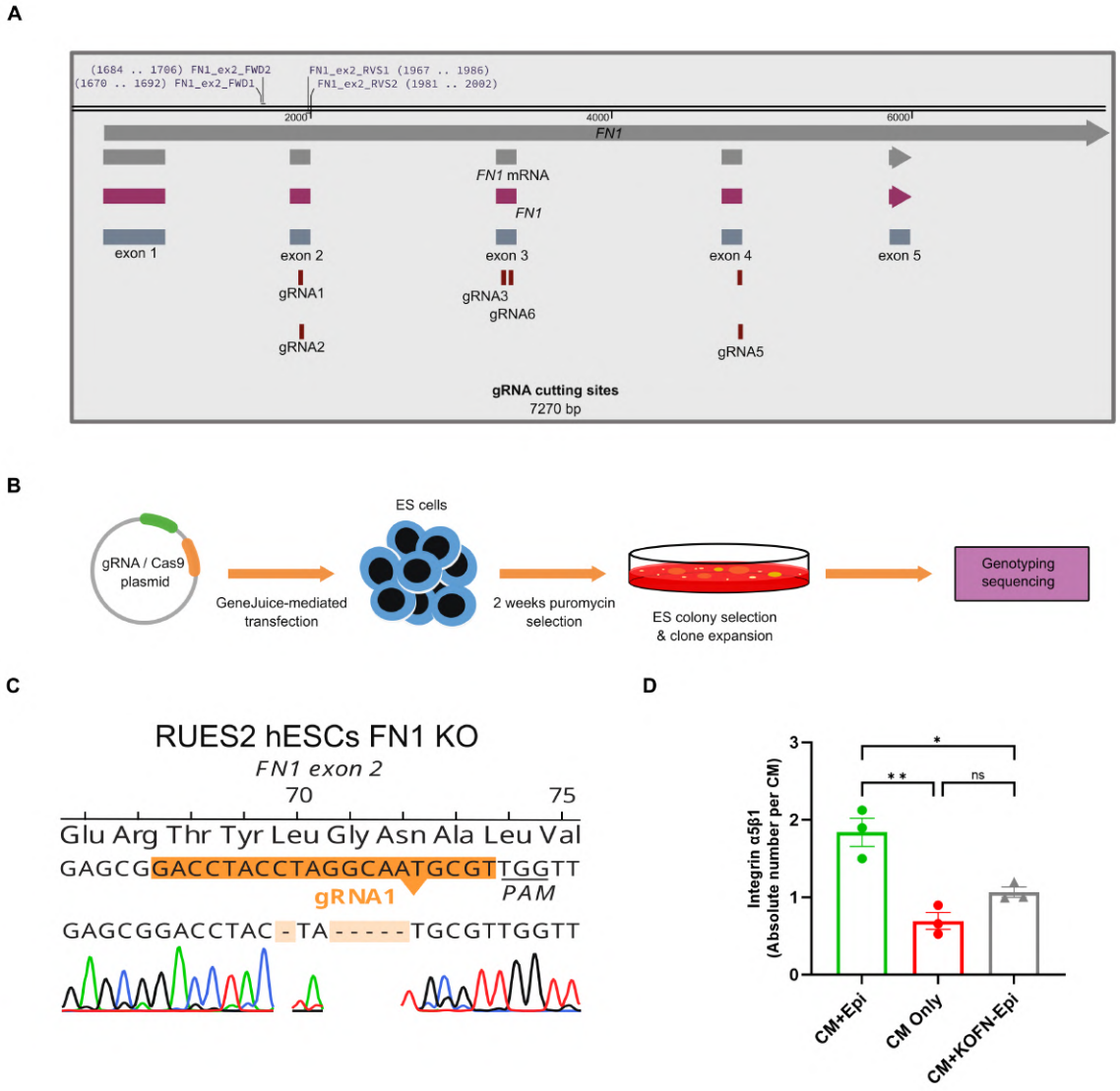

Supplementary Figure 2: Generation of Crispr-Cas9 Knockout FN cell line. (A) Overview of the design of gRNA incisions sites along FN exons. **(B)** Schematic of workflow for GeneJuice-mediated transfection of ES cells with Crispr-Cas9 gRNA to generate knockout-FN cell lines. **(C)** Genotyped Knock-out Fibronectin in Rues2 ES cells as aligned to WT-ES cells. **(D)** Quantification of Integrin α5β1 in 3D-EHTs containing, CM+EPI, CM only or CM+KOFN-EPI. Each experimental group included *N*=3 biological replicates.

Supplementary Figure 3: sOPTiKD-FN clones derivation after transfection with sOPTiKD vector.

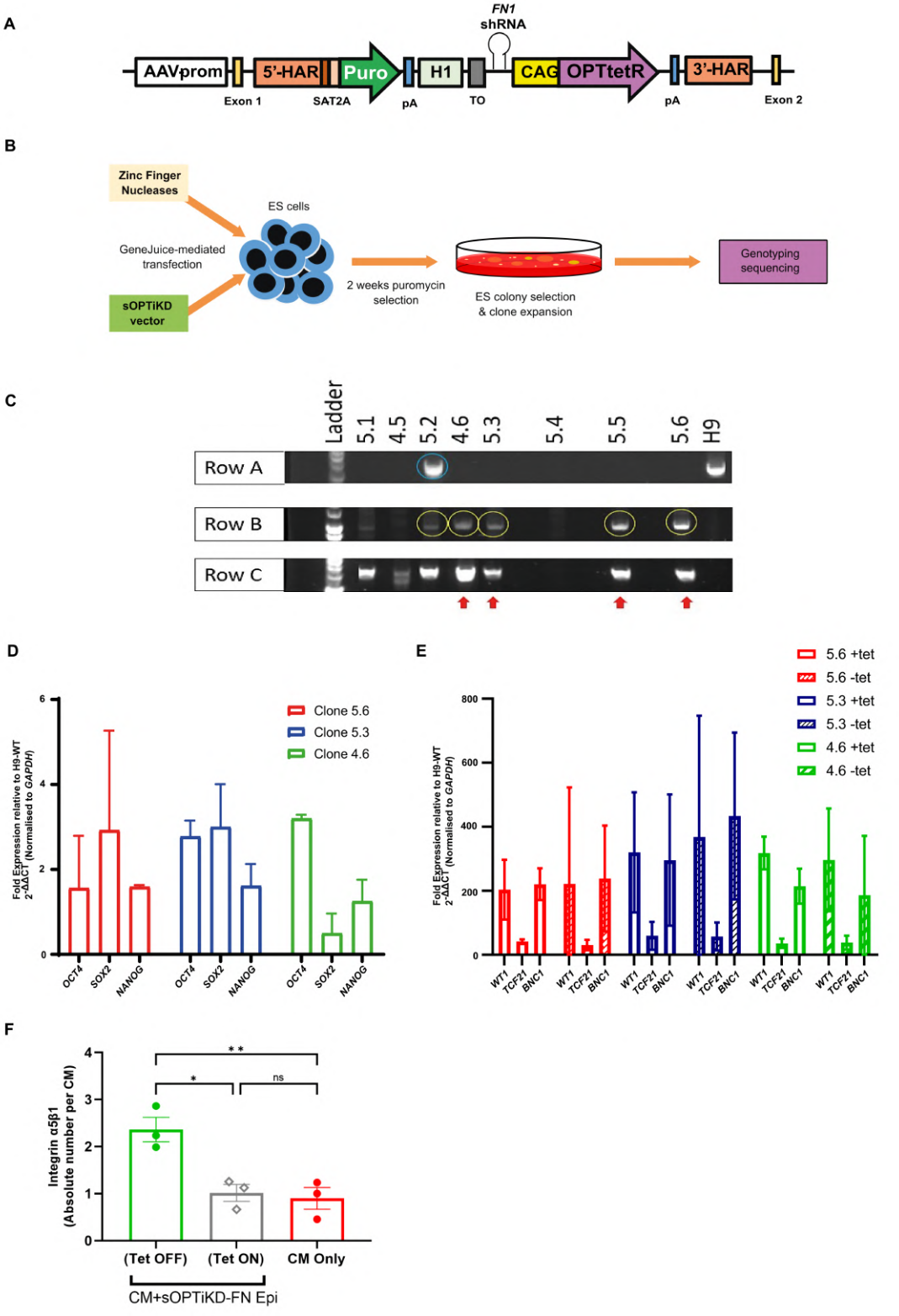

Supplementary Figure 3: sOPTiKD-FN clone derivation after transfection with sOPTiKD vector. (A) Schematic showing the transgenic allele that is generated via sOPTiKD

transfection of hPSC. AAV-prom, AAVS1 locus promoter; 5'-HAR/3'-HAR, 5' upstream and 3' downstream homology arms, respectively; SA, splice acceptor; T2A, self-cleaving T2A peptide; Puro, puromycin resistance; H1, H1 human RNA polymerase III promoter; TO, tet operon; pA, polyadenylation signal; CAG, CAG promoter; OPTtetR, optimised TET repressor. **(B)** Gene-Juice-mediated transfection strategy for sOPTiKD vector insertion within AAVS1 locus of ES cells, with subsequent colony selection and expansion for genotyping. **(C)** Genotyping gels of sOPTiKD clones. Row A is representative gel for detection of homozygous targeted clones; WT H9 give a band at 1692 bp, whereas no band indicates homozygous transgene integration. All clones except '5.2' (labelled 'het', blue circle) appear to be homozygous-targeted. Row B is representative gel for 5' vector integration, indicated by a gel band at 1103bp (yellow circle). Row C is representative gel for 3' vector integration, as indicated by gel band at 1447bp. In this example, clones 4.6, 5.3, 5.5, and 5.6 were homozygous-targeted with vector integration at 5' and 3' (red arrow).**(D)** All sOPTiKD clones had similar levels of pluripotency markers e.g. *OCT4*, *SOX2*, *NANOG*, prior to differentiation to epicardium. **(E)** Stable expression of key epicardial genes *WT1*, *TCF21* and *BNC1* in sOPTiKD-FN1 EPI following induction with tetracycline. **(F)** Quantification of Integrin α5β1 in 3D-EHTs containing, CM+sOPTiKD-FN EPI without or with tetracycline or containing CM alone. Each experimental group included *N*=3 biological replicates.

Supplementary Figure 4. Representative raw force and Ca^{2+}-traces.

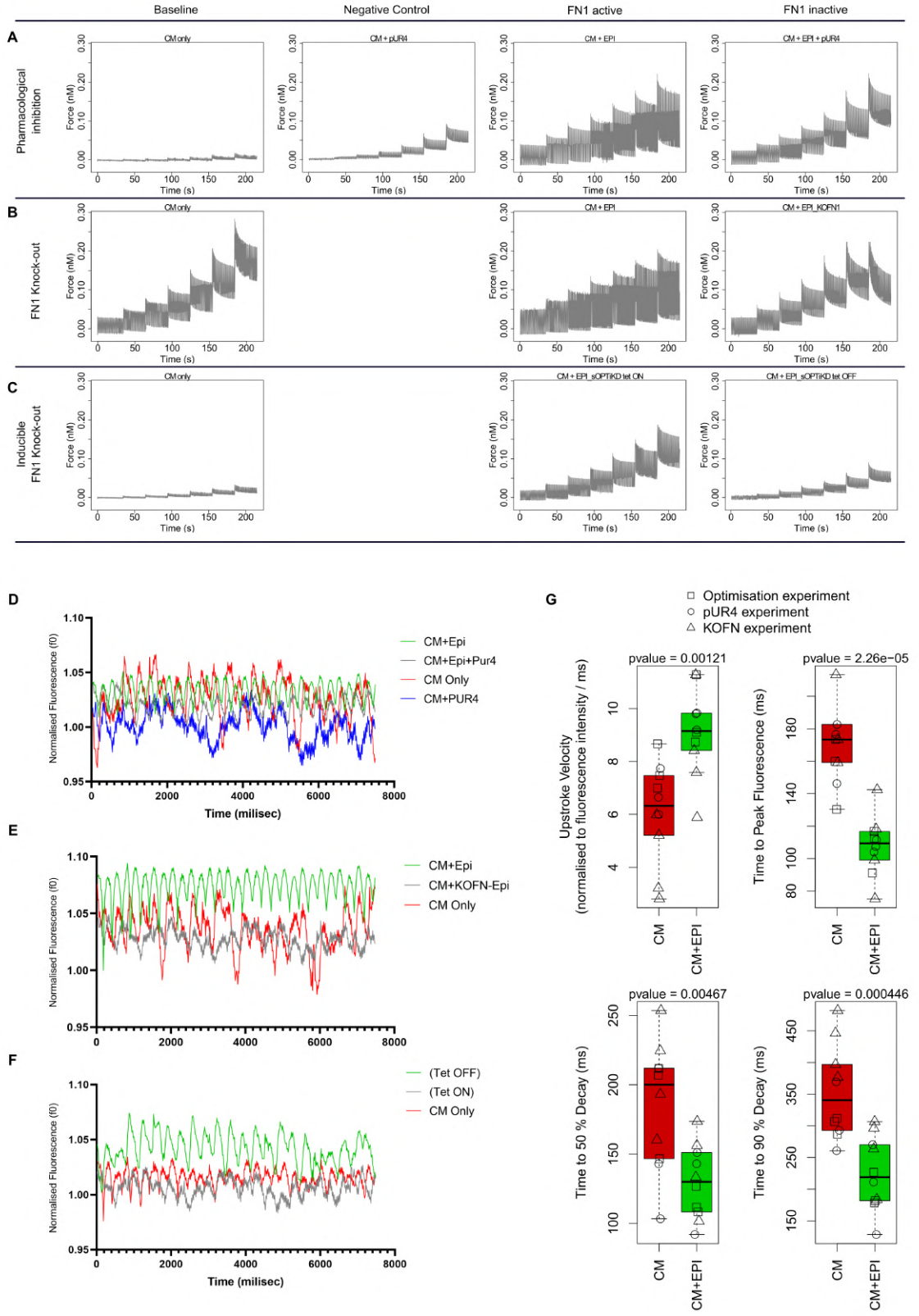

Supplementary Figure 4. Representative raw force and Ca^{2+}-traces. (A) Representative Frank-Starling traces of constructs containing CM only, CM+PUR4, CM+EPI or CM+EPI+PUR4. **(B)**

Representative Frank-Starling traces of constructs containing CM only, CM+EPI or CM+KOFN1 EPI. **(C)** CM only, CM+sOPTiKD-FN EPI (Tetracycline on) or CM+sOPTiKD-FN EPI (Tetracycline off). **(D)** Representative Ca^{2+}-curves of constructs containing CM+EPI, CM+EPI+PUR4, CM only or CM+PUR4. **(E)** Representative Ca^{2+}-curves of constructs containing CM+EPI, CM+KOFN EPI or CM only. **(F)** Representative Ca^{2+}-curves of constructs containing CM+sOPTiKD-FN EPI (Tetracycline off) or CM+sOPTiKD-FN EPI (Tetracycline on) or CM only. **(G)** Pooling Ca^{2+}-handling data from hPSC-CM or hPSC-CM+hPSC-EPI controls from the individual experiments results in significant differences between negative and positive control. Statistical significance was calculated using a two-tailed Welch's t-test, n = 10 (mean technical data pooled from experiments across n = 3, 3, and 4 individual differentiations).

Supplementary Figure 5. Technical validation of RNA sequencing.

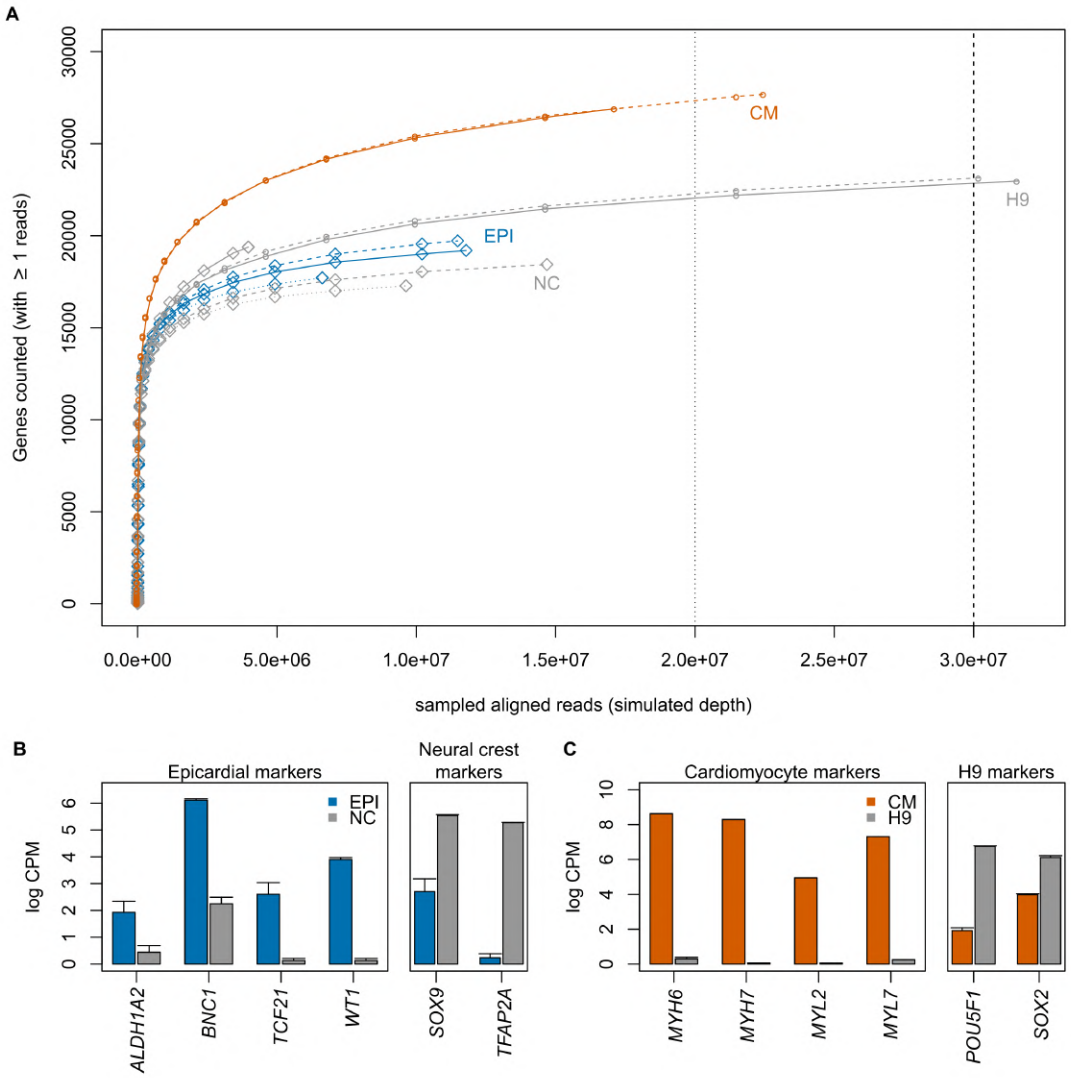

Supplementary Figure 5. Technical validation of RNA sequencing. (A) Sequencing depth saturation curves for all samples in both experiments. The hESC-NC (*n*=3) and hESC-EPI (*n*=3) samples were sequenced to depths of between 10 million and 24 million reads. The H9 (*n*=2) and the hESC-CM (*n*=2) samples were sequenced to depths of between 32 million and 44 million reads. The values plotted here show the number of reads sub-sampled up to and including the maximum number of reads obtained after filtering, trimming and alignment to genomic features. **(B)** Key positive markers used to identify hESC-EPIs and hESC-NCs. **(C)** Key positive markers used to identify hESC-CMs and H9s. Abbreviations: hESC, human embryonic stem cell; hESC-EPI, human embryonic stem cell-derived epicardial cells; hESC-CM, human embryonic stem cell-derived cardiomyocytes; hESC-NC, human embryonic stem cell-derived neural crest cells.

Supplementary Figure 6. Karyotypes of WT RUES2 and KOFN1 RUES2 hESC lines.

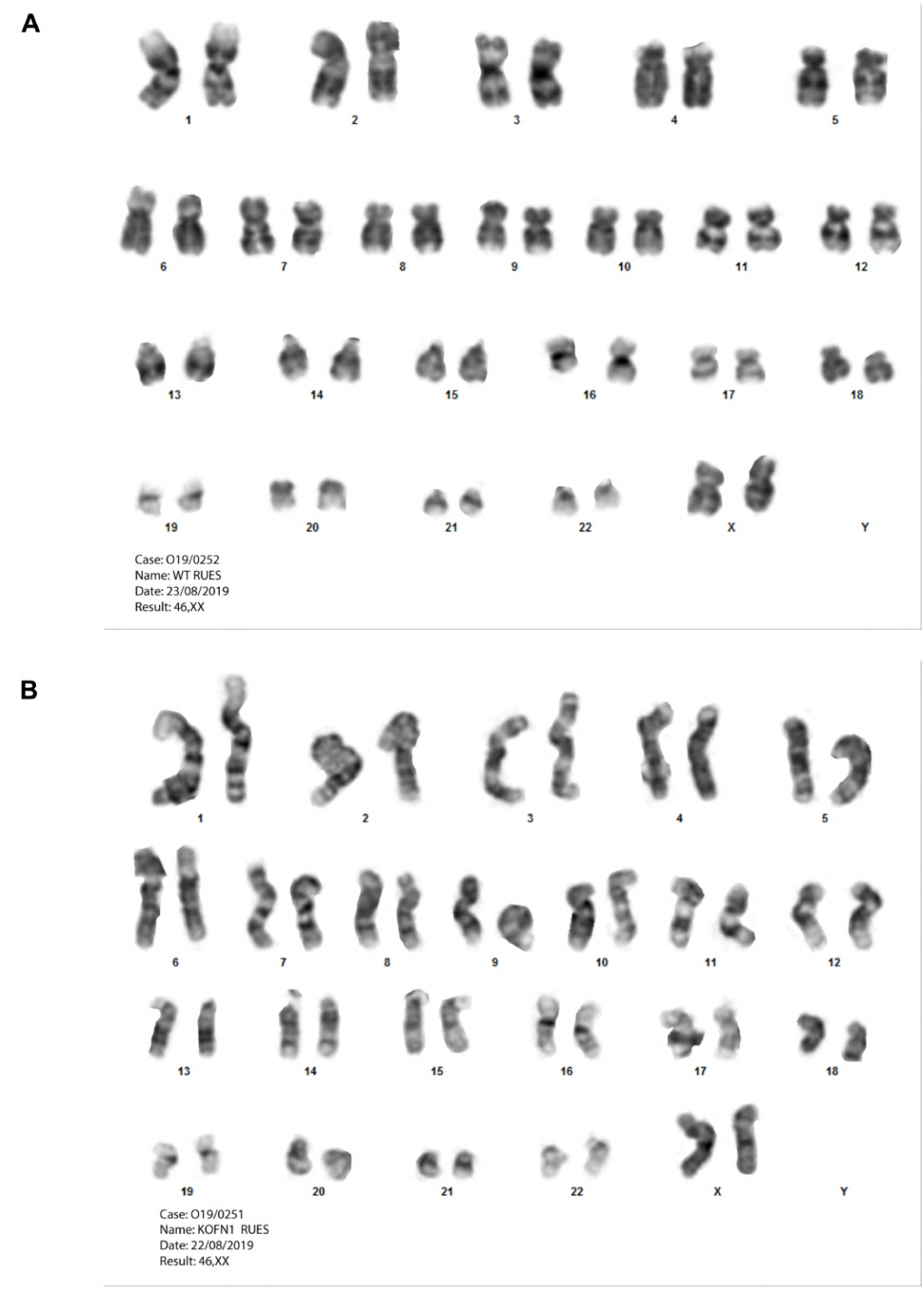

Supplementary Figure 6. Karyotypes of WT RUES2 and KOFN1 RUES2 hESC lines.

Supplemental Table 1. Putative paracrine interactions between hESC-epicardium secreted factors and hESC-cardiomyocyte membrane components as predicted and ranked by String-DB.

Epicardium		Cardiomyocytes				
Secreted Factor	L2FC	Membrane Receptor	L2FC	Interaction Score	Category	References
RSPO1	9.94	LGR5	3.69	997	Proliferation	Carmon et al., 2011; de Lau et al., 2011
NPPB	8.12	NPR3	4.66	964	Maturation	Moyes et al., 2020
NTF4	5.89	NTRK2	6.85	999	Angiogenesis	Wagner et al., 2005
IGF1	11.81	IGF1R	0.56	999	Proliferation	Knezevic et al., 2012; Huang et al., 2013
RSPO1	9.94	LGR4	1.61	998	Development; Proliferation; Survival	Carmon et al., 2011; Li Z et al., 2019
LY96	5.35	TLR4	5.95	999	Proliferation; Inflammation	Li N et al., 2019; Yucel et al., 2017
TGFB1	2.14	ITGB6	8.84	993	Proliferation; ECM regulation; Survival; Inflammation	Massague et al., 2012; Huang et al., 1996
RSPO1	9.94	RNF43	0.98	998	Regeneration; Proliferation	Szenker-Ravi et al., 2018; Hao et al., 2016; de Lau et al., 2014
IL1B	5.21	IL1R1	5.66	998	ECM regulation	Tulotta et al., 2019
FLT1	5.46	NRP1	5.18	995	Angiogenesis; Proliferation; Angiogenesis	Wang et al., 2019; Latil et al., 2000; Ding et al., 2019
DKK1	8.82	KREMEN1	1.51	995	Survival	Causeret et al., 2016
NRG1	2.74	ERBB4	7.25	998	Proliferation; Development; Maturation	Wadugu et al. 2012
IGFBP6	2.2	IGF2	7.25	997	Proliferation; Survival; Inflammation; Angiogenesis	Oliva et al., 2018; Micutkova et al., 2011; Kluge et al., 1997
BMP4	6.53	BMPR1B	1.91	997	Development	Kim et al., 2015; Goracy et al., 2012
IGF2	5.9	CLN5	2.09	813	Proliferation; Development; Metabolism	Huang et al., 2013; Savukoski et al., 1998; Qureshi et al., 2018
FN1	1.23	ITGB3	6.59	994	Angiogenesis; Proliferation; Survival	Brooks et al., 1994; Wei et al., 2020
INS-IGF2	5.95	SPN	1.41	766	Inflammation	Alisson-Silva et al., 2019; Cannon et al., 2008
TSLP	4.84	IL7R	2.43	995	Development	Peschon et al., 1994; Liu et al., 2007
BMP4	6.53	ACVR2A	0.72	984	Proliferation; Development	Kim et al., 2015; Rodriguez-Martinez et al., 2011
LIF	3.26	IL6ST	3.95	993	Survival	Fischer et al., 2007; Ishikawa et al., 1999

IL1B	5.21	IL1RAP	1.65	997	Inflammation	Huang et al., 1997; Cochain et al., 2018
IL1RAP	1.18	IL1R1	5.66	991	Inflammation; Proliferation	Huang et al., 1997; Mitchell et al., 2018
NTF4	5.89	BDNF	0.82	993	Development	Feng et al., 2015; Donovan et al., 2000
IL18	3.81	IL18R1	2.47	995	Maturation; Inflammation; Proliferation	Chandrasekar et al., 2005a; Mallat et al., 2004; Chandrasekar et al., 2005b
IL1R1	4.54	IL1RAP	1.65	991	Inflammation	Huang et al., 1997; Mitchell et al., 2018
F10	4.41	ASPH	1.01	800	Metabolism; EMT regulation	Li et al., 2015; Gundogan et al., 2007
TGFB1	2.14	ITGAV	2.91	991	Angiogenesis	McCarty et al., 2005; Arnold et al., 2012
EGFR	0.86	EPGN	4.15	923	Proliferation	Taniguchi et al., 2011
IL6ST	3.7	IL6R	1.19	991	Inflammation; Development	Swerdlow et al., 2012
APOC1	3.76	MPC2	0.62	707	Survival	Fernandez-Caggiano et al., 2016
FN1	1.23	ITGAV	2.91	995	ECM regulation & Proliferation	Ding et al., 2017
FN1	1.23	EGFR	2.73	947	ECM regulation	Berger et al., 2020; Takashima et al., 2019
PVR	0.87	TIGIT	3.09	995	Inflammation	Stanietsky et al., 2009; Yu et al., 2009
COLQ	1.77	PLOD2	1.86	834	ECM regulation	Helmer et al., 2013
HGF	2.74	MET	0.62	999	Survival; Angiogenesis; Proliferation; Inflammation	Gallo et al., 2014; Gallo et al., 2015
EMC10	0.41	TRDN	2.94	719	Metabolism; Development; Angiogenesis	Reboll et al., 2017; Kobayashi et al, 1999; Knollmann et al., 2009
TFRC	1.94	HFE	1.24	998	Metabolism	Benyamin et al., 2014
EGFR	0.86	EREG	2.16	998	Proliferation	Shirakata et al., 2000
PDGFB	1.83	PDGFRB	0.94	998	Survival; Development; Regeneration	Vantler et al., 2010; Van den Akker et al., 2008; Zymek et al., 2006; Tuuminen et al., 2016
EFNA1	1.98	EPHA2	0.73	999	Angiogenesis	Kataoka et al., 2004; Cui et al., 2010
EGFR	0.86	EGF	1.66	999	Development	Schwarz et al., 2018; Samsa et al., 2016; De Pasquale et al., 2018
FGF2	1.55	FGFR3	0.89	993	Survival	Okada et al., 2019
PCDHA10	1.19	PCDHA9	1.18	831	Development	Yagi et al., 2018; Ferreri et al., 2010
TIMP1	1.08	MMP14	0.85	980	ECM regulation	Frahs et al., 2019; Sato et al., 1994
PCDHA10	1.19	PCDHA6	0.68	834	Inflammation	Greliche et al., 2012

AGRN	0.8	LRP4	0.75	995	Development	Kaplan et al., 2019
ANXA2	0.45	RPS6KA3	0.45	711	Metabolism	Lamore et al., 2017; Merienne et al., 1999

NRG1	2.74	EGFR	2.73	591
IGF2	5.9	IGF1R	0.56	522
FN1	1.23	HGF	2.74	518
BDNF	0.82	NTRK2	6.85	472
NTRK2	6.85	EGFR	2.73	431
EGFR	2.73	MET	0.62	418
EGFR	0.86	IGF1R	0.56	418
ITGB3	6.59	PDGFRB	0.94	407
EGFR	0.86	PDGFRB	0.94	405

Alisson-Silva F, Mantuano NR, Lopes AL, Vasconcelos-Dos-Santos A, Vale AM, Costa MM, et al. CD43 sialoglycoprotein modulates cardiac inflammation and murine susceptibility to Trypanosoma cruzi infection. Scientific reports. 2019;9(1):8628.

Arnold TD, Ferrero GM, Qiu H, Phan IT, Akhurst RJ, Huang EJ, et al. Defective retinal vascular endothelial cell development as a consequence of impaired integrin alphaVbeta8-mediated activation of transforming growth factor-beta. The Journal of neuroscience : the official journal of the Society for Neuroscience. 2012;32(4):1197-206.

Benyamin B, Esko T, Ried JS, Radhakrishnan A, Vermeulen SH, Traglia M, et al. Novel loci affecting iron homeostasis and their effects in individuals at risk for hemochromatosis. Nature communications. 2014;5:4926.

Berger AJ, Renner CM, Hale I, Yang X, Ponik SM, Weisman PS, et al. Scaffold stiffness influences breast cancer cell invasion via EGFR-linked Mena upregulation and matrix remodeling. Matrix biology: journal of the International Society for Matrix Biology. 2020;85-86:80-93.

Brooks PC, Clark RA, Cheresh DA. Requirement of vascular integrin alpha v beta 3 for angiogenesis. Science (New York, NY). 1994;264(5158):569-71.

Cannon JL, Collins A, Mody PD, Balachandran D, Henriksen KJ, Smith CE, et al. CD43 regulates Th2 differentiation and inflammation. Journal of immunology (Baltimore, Md : 1950). 2008;180(11):7385-93.

cardiomyocyte-enriched microRNA, miR-378, targets insulin-like growth factor 1 receptor: implications in postnatal cardiac remodeling and cell survival. The Journal of biological chemistry. 2012;287(16):12913-26. Huang Y, Harrison MR, Osorio A, Kim J, Baugh A, Duan C, et al. Igf Signaling is Required for Cardiomyocyte Proliferation during Zebrafish Heart Development and Regeneration. PloS one. 2013;8(6):e67266.

Carmon KS, Gong X, Lin Q, Thomas A, Liu Q. R-spondins function as ligands of the orphan receptors LGR4 and LGR5 to regulate Wnt/beta-catenin signaling. Proceedings of the National Academy of Sciences of the United States of America. 2011;108(28):11452-7.

Causeret F, Sumia I, Pierani A. Kremen1 and Dickkopf1 control cell survival in a Wnt-independent manner. Cell death and differentiation. 2016;23(2):323-32.

Chandrasekar B, Mummidi S, Claycomb WC, Mestril R, Nemer M. Interleukin-18 is a pro-hypertrophic cytokine that acts through a phosphatidylinositol 3-kinase-

phosphoinositide-dependent kinase-1-Akt-GATA4 signaling pathway in cardiomyocytes. The Journal of biological chemistry. 2005;280(6):4553-67.
Chandrasekar B, Mummidi S, Valente AJ, Patel DN, Bailey SR, Freeman GL, et al. The pro-atherogenic cytokine interleukin-18 induces CXCL16 expression in rat aortic smooth muscle cells via MyD88, interleukin-1 receptor-associated kinase, tumor necrosis factor receptor-associated factor 6, c-Src, phosphatidylinositol 3-kinase, Akt, c-Jun N-terminal kinase, and activator protein-1 signaling. The Journal of biological chemistry. 2005;280(28):26263-77.
Cochain C, Vafadarnejad E, Arampatzi P, Pelisek J, Winkels H, Ley K, et al. Single-Cell RNA-Seq Reveals the Transcriptional Landscape and Heterogeneity of Aortic Macrophages in Murine Atherosclerosis. Circulation research. 2018;122(12):1661-74.
Cui XD, Lee MJ, Yu GR, Kim IH, Yu HC, Song EY, et al. EFNA1 ligand and its receptor EphA2: potential biomarkers for hepatocellular carcinoma. International journal of cancer. 2010;126(4):940-9.
de Lau W, Barker N, Low TY, Koo BK, Li VS, Teunissen H, et al. Lgr5 homologues associate with Wnt receptors and mediate R-spondin signalling. Nature. 2011;476(7360):293-7.
de Lau W, Peng WC, Gros P, Clevers H. The R-spondin/Lgr5/Rnf43 module: regulator of Wnt signal strength. Genes & development. 2014;28(4):305-16.
De Pasquale V, Pezone A, Sarogni P, Tramontano A, Schiattarella GG, Avvedimento VE, et al. EGFR activation triggers cellular hypertrophy and lysosomal disease in NAGLU-depleted cardiomyoblasts, mimicking the hallmarks of mucopolysaccharidosis IIIB. Cell death & disease. 2018;9(2):40.
Ding Y, Pan Y, Liu S, Jiang F, Jiao J. Elevation of MiR-9-3p suppresses the epithelial-mesenchymal transition of nasopharyngeal carcinoma cells via down-regulating FN1, ITGB1 and ITGAV. Cancer biology & therapy. 2017;18(6):414-24.
Ding Z, Zhu J, Zeng Y, Du W, Zhang Y, Tang H, et al. The regulation of Neuropilin 1 expression by miR-338-3p promotes non-small cell lung cancer via changes in EGFR signaling. Molecular carcinogenesis. 2019;58(6):1019-32.
Dispensable for Cardiac Trabeculation in Zebrafish. PloS one. 2016;11(11):e0166734.
Donovan MJ, Lin MI, Wiegn P, Ringstedt T, Kraemer R, Hahn R, et al. Brain derived neurotrophic factor is an endothelial cell survival factor required for intramyocardial vessel stabilization. Development (Cambridge, England). 2000;127(21):4531-40.
Feng N, Huke S, Zhu G, Tocchetti CG, Shi S, Aiba T, et al. Constitutive BDNF/TrkB signaling is required for normal cardiac contraction and relaxation. Proceedings of the National Academy of Sciences of the United States of America. 2015;112(6):1880-5.
Fernandez-Caggiano M, Prysyazhna O, Barallobre-Barreiro J, CalvinoSantos R, Aldama Lopez G, Generosa Crespo-Leiro M, et al. Analysis of Mitochondrial Proteins in the Surviving Myocardium after Ischemia Identifies Mitochondrial Pyruvate Carrier Expression as Possible Mediator of Tissue Viability. Molecular & cellular proteomics: MCP. 2016;15(1):246-55.
Ferreri AJ, Illerhaus G, Zucca E, Cavalli F. Flows and flaws in primary central nervous system lymphoma. Nature reviews Clinical oncology. 2010;7(8):doi:10.1038/nrclinonc.2010.9-c1; author reply doi:10:1038/nrclinonc.2010.9-c2.
Fischer P, Hilfiker-Kleiner D. Survival pathways in hypertrophy and heart failure: the gp130-STAT3 axis. Basic research in cardiology. 2007;102(4):279-97.
Frahs SM, Reeck JC, Yocham KM, Frederiksen A, Fujimoto K, Scott CM, et al. Prechondrogenic ATDC5 Cell Attachment and Differentiation on Graphene Foam;

Modulation by Surface Functionalization with Fibronectin. ACS applied materials & interfaces. 2019;11(45):41906-24.
Gallo S, Sala V, Gatti S, Crepaldi T. Cellular and molecular mechanisms of HGF/Met in the cardiovascular system. Clinical science (London, England : 1979). 2015;129(12):1173-93.
Gallo S, Sala V, Gatti S, Crepaldi T. HGF/Met Axis in Heart Function and Cardioprotection. Biomedicines. 2014;2(4):247-62.
Goracy I, Safranow K, Dawid G, Skonieczna-Zydecka K, Kaczmarczyk M, Goracy J, et al. Common genetic variants of the BMP4, BMPR1A, BMPR1B, and ACVR1 genes, left ventricular mass, and other parameters of the heart in newborns. Genetic testing and molecular biomarkers. 2012;16(11):1309-16.
Greliche N, Zeller T, Wild PS, Rotival M, Schillert A, Ziegler A, et al. Comprehensive exploration of the effects of miRNA SNPs on monocyte gene expression. PloS one. 2012;7(9):e45863.
Gundogan F, Elwood G, Greco D, Rubin LP, Pinar H, Carlson RI, et al. Role of aspartyl-(asparaginyl) beta-hydroxylase in placental implantation: Relevance to early pregnancy loss. Human pathology. 2007;38(1):50-9.
Hao HX, Jiang X, Cong F. Control of Wnt Receptor Turnover by R-spondin-ZNRF3/RNF43 Signaling Module and Its Dysregulation in Cancer. Cancers. 2016;8(6).
Helmer RA, Martinez-Zaguilan R, Dertien JS, Fulford C, Foreman O, Peiris V, et al. Helicase-like transcription factor (Hltf) regulates G2/M transition, Wt1/Gata4/Hif-1a cardiac transcription networks, and collagen biogenesis. PloS one. 2013;8(11):e80461.
Huang J, Gao X, Li S, Cao Z. Recruitment of IRAK to the interleukin 1 receptor complex requires interleukin 1 receptor accessory protein. Proceedings of the National Academy of Sciences of the United States of America. 1997;94(24):12829-32.
Huang XZ, Wu JF, Cass D, Erle DJ, Corry D, Young SG, et al. Inactivation of the integrin beta 6 subunit gene reveals a role of epithelial integrins in regulating inflammation in the lung and skin. The Journal of cell biology. 1996;133(4):921-8.
Ishikawa M, Saito Y, Miyamoto Y, Harada M, Kuwahara K, Ogawa E, et al. A heart-specific increase in cardiotrophin-1 gene expression precedes the establishment of ventricular hypertrophy in genetically hypertensive rats. Journal of hypertension. 1999;17(6):807-16.
Kaplan NA, Wang W, Christiaen L. Initial characterization of Wnt-Tcf functions during Ciona heart development. Developmental biology. 2019;448(2):199-209.
Kataoka H, Igarashi H, Kanamori M, Ihara M, Wang JD, Wang YJ, et al. Correlation of EPHA2 overexpression with high microvessel count in human primary colorectal cancer. Cancer science. 2004;95(2):136-41.
Kim MS, Horst A, Blinka S, Stamm K, Mahnke D, Schuman J, et al. Activin-A and Bmp4 levels modulate cell type specification during CHIR-induced cardiomyogenesis. PloS one. 2015;10(2):e0118670.
Kluge A, Zimmermann R, Weihrauch D, Mohri M, Sack S, Schaper J, et al. Coordinate expression of the insulin-like growth factor system after microembolisation in porcine heart. Cardiovascular research. 1997;33(2):324-31.
Knezevic I, Patel A, Sundaresan NR, Gupta MP, Solaro RJ, Nagalingam RS, et al. A novel
Knollmann BC. New roles of calsequestrin and triadin in cardiac muscle. The Journal of physiology. 2009;587(Pt 13):3081-7.
Kobayashi YM, Jones LR. Identification of triadin 1 as the predominant triadin isoform expressed in mammalian myocardium. The Journal of biological chemistry. 1999;274(40):28660-8.

Lamore SD, Ahlberg E, Boyer S, Lamb ML, Hortigon-Vinagre MP, Rodriguez V, et al. Deconvoluting Kinase Inhibitor Induced Cardiotoxicity. Toxicological sciences : an official journal of the Society of Toxicology. 2017;158(1):213-26.
Latil A, Bieche I, Pesche S, Valeri A, Fournier G, Cussenot O, et al. VEGF overexpression in clinically localized prostate tumors and neuropilin-1 overexpression in metastatic forms. International journal of cancer. 2000;89(2):167-71.
Li L, Mirza S, Richardson SJ, Gallant EM, Thekkedam C, Pace SM, et al. A new cytoplasmic interaction between junctin and ryanodine receptor Ca2+ release channels. Journal of cell science. 2015;128(5):951-63.
Li N, Xu H, Ou Y, Feng Z, Zhang Q, Zhu Q, et al. LPS-induced CXCR7 expression promotes gastric Cancer proliferation and migration via the TLR4/MD-2 pathway. Diagnostic pathology. 2019;14(1):3.
Li Z, Liu S, Lou J, Mulholland M, Zhang W. LGR4 protects hepatocytes from injury in mouse. American journal of physiology Gastrointestinal and liver physiology. 2019;316(1):G123-g31.
Liu YJ, Soumelis V, Watanabe N, Ito T, Wang YH, Malefyt Rde W, et al. TSLP: an epithelial cell cytokine that regulates T cell differentiation by conditioning dendritic cell maturation. Annual review of immunology. 2007;25:193-219.
Mallat Z, Heymes C, Corbaz A, Logeart D, Alouani S, Cohen-Solal A, et al. Evidence for altered interleukin 18 (IL)-18 pathway in human heart failure. FASEB journal : official publication of the Federation of American Societies for Experimental Biology. 2004;18(14):1752-4.
Massague J. TGFbeta signalling in context. Nature reviews Molecular cell biology. 2012;13(10):616-30.
McCarty JH, Lacy-Hulbert A, Charest A, Bronson RT, Crowley D, Housman D, et al. Selective ablation of alphav integrins in the central nervous system leads to cerebral hemorrhage, seizures, axonal degeneration and premature death. Development (Cambridge, England). 2005;132(1):165-76.
Merienne K, Jacquot S, Pannetier S, Zeniou M, Bankier A, Gecz J, et al. A missense mutation in RPS6KA3 (RSK2) responsible for non-specific mental retardation. Nature genetics. 1999;22(1):13-4.
Micutkova L, Diener T, Li C, Rogowska-Wrzesinska A, Mueck C, Huetter E, et al. Insulin-like growth factor binding protein-6 delays replicative senescence of human fibroblasts. Mechanisms of ageing and development. 2011;132(10):468-79.
Mitchell K, Barreyro L, Todorova TI, Taylor SJ, Antony-Debre I, Narayanagari SR, et al. IL1RAP potentiates multiple oncogenic signaling pathways in AML. The Journal of experimental medicine. 2018;215(6):1709-27.
Moyes AJ, Chu SM, Aubdool AA, Dukinfield MS, Margulies KB, Bedi KC, et al. C-type natriuretic peptide co-ordinates cardiac structure and function. European heart journal. 2020;41(9):1006-20.
Okada T, Enkhjargal B, Travis ZD, Ocak U, Tang J, Suzuki H, et al. FGF-2 Attenuates Neuronal Apoptosis via FGFR3/PI3k/Akt Signaling Pathway After Subarachnoid Hemorrhage. Molecular neurobiology. 2019;56(12):8203-19.
Oliva CR, Halloran B, Hjelmeland AB, Vazquez A, Bailey SM, Sarkaria JN, et al. IGFBP6 controls the expansion of chemoresistant glioblastoma through paracrine IGF2/IGF-1R signaling. Cell communication and signaling : CCS. 2018;16(1):61.
Peschon JJ, Morrissey PJ, Grabstein KH, Ramsdell FJ, Maraskovsky E, Gliniak BC, et al. Early lymphocyte expansion is severely impaired in interleukin 7 receptor-deficient mice. The Journal of experimental medicine. 1994;180(5):1955-60.
Qureshi YH, Patel VM, Berman DE, Kothiya MJ, Neufeld JL, Vardarajan B, et al. An Alzheimer's Disease-Linked Loss-of-Function CLN5 Variant Impairs Cathepsin D

Maturation, Consistent with a Retromer Trafficking Defect. Molecular and cellular biology. 2018;38(20).
Reboll MR, Korf-Klingebiel M, Klede S, Polten F, Brinkmann E, Reimann I, et al. EMC10 (Endoplasmic Reticulum Membrane Protein Complex Subunit 10) Is a Bone Marrow-Derived Angiogenic Growth Factor Promoting Tissue Repair After Myocardial Infarction. Circulation. 2017;136(19):1809-23.
Rodriguez-Martinez A, Alarmo EL, Saarinen L, Ketolainen J, Nousiainen K, Hautaniemi S, et al. Analysis of BMP4 and BMP7 signaling in breast cancer cells unveils time-dependent transcription patterns and highlights a common synexpression group of genes. BMC medical genomics. 2011;4:80.
Samsa LA, Ito CE, Brown DR, Qian L, Liu J. IgG-Containing Isoforms of Neuregulin-1 Are
Sato H, Takino T, Okada Y, Cao J, Shinagawa A, Yamamoto E, et al. A matrix metalloproteinase expressed on the surface of invasive tumour cells. Nature. 1994;370(6484):61-5.
Savukoski M, Klockars T, Holmberg V, Santavuori P, Lander ES, Peltonen L. CLN5, a novel gene encoding a putative transmembrane protein mutated in Finnish variant late infantile neuronal ceroid lipofuscinosis. Nature genetics. 1998;19(3):286-8.
Schwarz B, Hollfelder D, Scharf K, Hartmann L, Reim I. Diversification of heart progenitor cells by EGF signaling and differential modulation of ETS protein activity. ELife. 2018;7.
Shirakata Y, Komurasaki T, Toyoda H, Hanakawa Y, Yamasaki K, Tokumaru S, et al. Epiregulin, a novel member of the epidermal growth factor family, is an autocrine growth factor in normal human keratinocytes. The Journal of biological chemistry. 2000;275(8):5748-53. Vantler M, Karikkineth BC, Naito H, Tiburcy M, Didie M, Nose M, et al. PDGF-BB protects cardiomyocytes from apoptosis and improves contractile function of engineered heart tissue. Journal of molecular and cellular cardiology. 2010;48(6):1316-23.
Stanietsky N, Simic H, Arapovic J, Toporik A, Levy O, Novik A, et al. The interaction of TIGIT with PVR and PVRL2 inhibits human NK cell cytotoxicity. Proceedings of the National Academy of Sciences of the United States of America. 2009;106(42):17858-63.
Swerdlow DI, Holmes MV, Kuchenbaecker KB, Engmann JE, Shah T, Sofat R, et al. The interleukin-6 receptor as a target for prevention of coronary heart disease: a mendelian randomisation analysis. Lancet (London, England). 2012;379(9822):1214-24.
Szenker-Ravi E, Altunoglu U, Leushacke M, Bosso-Lefevre C, Khatoo M, Thi Tran H, et al. RSPO2 inhibition of RNF43 and ZNRF3 governs limb development independently of LGR4/5/6. Nature. 2018;557(7706):564-9.
Takashima Y, Kawaguchi A, Yamanaka R. Promising Prognosis Marker Candidates on the Status of Epithelial-Mesenchymal Transition and Glioma Stem Cells in Glioblastoma. Cells. 2019;8(11).
Taniguchi K, Yamamoto S, Aoki S, Toda S, Izuhara K, Hamasaki Y. Epigen is induced during the interleukin-13-stimulated cell proliferation in murine primary airway epithelial cells. Experimental lung research. 2011;37(8):461-70.
Tulotta C, Lefley DV, Freeman K, Gregory WM, Hanby AM, Heath PR, et al. Endogenous Production of IL1B by Breast Cancer Cells Drives Metastasis and Colonization of the Bone Microenvironment. Clinical cancer research : an official journal of the American Association for Cancer Research. 2019;25(9):2769-82.
Tuuminen R, Dashkevich A, Keranen MA, Raissadati A, Krebs R, Jokinen JJ, et al. Platelet-derived Growth Factor-B Protects Rat Cardiac Allografts From Ischemia-reperfusion Injury. Transplantation. 2016;100(2):303-13.

Van den Akker NM, Winkel LC, Nisancioglu MH, Maas S, Wisse LJ, Armulik A, et al. PDGF-B signaling is important for murine cardiac development: its role in developing atrioventricular valves, coronaries, and cardiac innervation. Developmental dynamics: an official publication of the American Association of Anatomists. 2008;237(2):494-503.

Wadugu B, Kuhn B. The role of neuregulin/ErbB2/ErbB4 signaling in the heart with special focus on effects on cardiomyocyte proliferation. American journal of physiology Heart and circulatory physiology. 2012;302(11):H2139-47.

Wagner N, Wagner KD, Theres H, Englert C, Schedl A, Scholz H. Coronary vessel development requires activation of the TrkB neurotrophin receptor by the Wilms' tumor transcription factor Wt1. Genes & development. 2005;19(21):2631-42.

Wang L, Feng Y, Xie X, Wu H, Su XN, Qi J, et al. Neuropilin-1 aggravates liver cirrhosis by promoting angiogenesis via VEGFR2-dependent PI3K/Akt pathway in hepatic sinusoidal endothelial cells. EBioMedicine. 2019;43:525-36.

Wei L, Zhou Q, Tian H, Su Y, Fu GH, Sun T. Integrin beta3 promotes cardiomyocyte proliferation and attenuates hypoxia-induced apoptosis via regulating the PTEN/Akt/mTOR and ERK1/2 pathways. International journal of biological sciences. 2020;16(4):644-54.

Wooldridge LK, Johnson SE, Cockrum RR, Ealy AD. Interleukin-6 requires JAK to stimulate inner cell mass expansion in bovine embryos. Reproduction (Cambridge, England). 2019;158(4):303-12.

Yagi H, Liu X, Gabriel GC, Wu Y, Peterson K, Murray SA, et al. The Genetic Landscape of Hypoplastic Left Heart Syndrome. Pediatric cardiology. 2018;39(6):1069-81.

Yu X, Harden K, Gonzalez LC, Francesco M, Chiang E, Irving B, et al. The surface protein TIGIT suppresses T cell activation by promoting the generation of mature immunoregulatory dendritic cells. Nature immunology. 2009;10(1):48-57.

Yucel G, Zhao Z, El-Battrawy I, Lan H, Lang S, Li X, et al. Lipopolysaccharides induced inflammatory responses and electrophysiological dysfunctions in human-induced pluripotent stem cell derived cardiomyocytes. Scientific reports. 2017;7(1):2935.

Zymek P, Bujak M, Chatila K, Cieslak A, Thakker G, Entman ML, et al. The role of platelet-derived growth factor signaling in healing myocardial infarcts. Journal of the American College of Cardiology. 2006;48(11):2315-23.

Supplemental Experimental Procedures

Cell Differentiations and Preparations

hESC-derived epicardium

Epicardial cells were differentiated from GFP-transgenic hESCs (H9, WiCell, Madison) as previously described (Iyer et al., 2015). hESCs were maintained in a chemically defined medium composed of bovine serum albumin fraction A (CDM-BSA), with Activin-A (10 ng/mL, R&D Systems) and FGF2 (12 ng/ml, R&D Systems) on gelatin-coated plates. Cell colonies were passaged when they reached ~70% confluence. Chemically defined media contained IMDM (250 ml, Life Technologies), Ham's F12 (250 ml, Life Technologies), penicillin-streptomycin (Sigma, 1%), Insulin (7 µg/ml, Roche), transferrin (15 µg/ml, Roche), chemically defined lipid concentrate (Life Technologies) and monothioglycerol (450 µM, Sigma). All subsequent differentiations were conducted in CDM-PVA, containing polyvinyl alcohol (PVA, 1 mg/ml, Sigma) instead of BSA (Iyer et al., 2015). Early mesoderm differentiation started with CDM-PVA, FGF2 (20 ng/ml), LY294002 (10 µM, Sigma) and BMP4 (10 ng/ml, R&D) for 1.5 days. Lateral mesoderm differentiation was initiated in CDM-PVA, FGF2 (20 ng/ml) and BMP4 (50 ng/ml) for 3.5 days. To differentiate into epicardium, cells were singly suspended in CDM-PVA, WNT3A (25 ng/ml, R&D), BMP4 (50 ng/ml) and RA (4 µM, Sigma), then replated at a density of 2.5 x 10^4 cells/cm^2 for exactly ten days with a full media change after five days.

RUES2-derived epicardium

To differentiate epicardial cells from a different cell line (RUES2, female line, Rockefeller University, NIH registry number 0013), a few modifications to the step above was undertaken. RUES2 cell line was maintained in feeder-free, irradiated mouse embryonic fibroblast (MEF)-conditioned medium containing bFGF (4 ng/ml, Peprotech) with single-cell passaging when ~70% confluent. Lateral mesoderm differentiation was conducted in CDM-PVA, FGF2 (20 ng/ml) and BMP4 (50 ng/ml) for a maximum of 2.5 days. To differentiate into epicardium, cells were singly suspended in CDM-PVA, WNT3A (25 ng/ml, R&D), BMP4 (50 ng/ml) and RA (4 µM, Sigma) at a replating density of 1.5 x 10^4 cells/cm^2 for ten days with media change every five days. All re-plating of the cells included Rock inhibitor (10 µM, Y-27632) in

addition to the cytokines described above. Additionally, SB431542 (2 μM) was introduced into the culture medium on Day 3 after epicardium differentiation.

hESC-derived cardiomyocytes

hESC-derived CMs were generated with the ABCX method as previously described (Bargehr et al., 2019) As above, hESCs (RUES2, female line, Rockefeller University, NIH registry number 0013) were maintained in feeder-free, irradiated mouse embryonic fibroblast (MEF)-conditioned medium containing bFGF (4 ng/ml, Peprotech) with single-cell passaging when ~70% confluent. Cells were seeded as single cells (1 x 10^5/cm^2) on Matrigel-coated (BD 449) plates with media enriched with Chiron 99021 (1 μM, Cayman Chemical) and ROCK inhibitor (10 μM, Y-27632). On Day 0, the RPMI medium was supplemented with 1X B27 minus insulin (Invitrogen) and Activin A (100 ng/ml) for 18 hours. On day 1, cells were fed with RPMI media plus B27 containing BMP4 (5 ng/ml) and Chiron 99021 (1 μM) for 2 days. On day 3, the media was exchanged with RPMI medium plus B27 and Xav 939 (1 μM, Tocris). On day 5, the media was switched to RPMI medium plus B27. On day 7, the media was exchanged with RPMI plus B27 with insulin (Invitrogen). Subsequently, this media was replaced every other day until D28 and harvested for 3D-EHTs generation.

Generation of 3D-EHTs

The 3D-EHTs wells were fabricated using polydimethylsiloxane (PDMS) (PDMS, Sylgard 184; Dow Corning, Midland, MI). PDMS linker and base were mixed in a 1:10 mass-ratio and poured into laser-etched acrylic negative templates, which composed of four wells measuring 3x8x2 mm each. Each well also contained 2x1mm diameter posts positioned 3mm from each other. PDMS was baked at 65°C overnight, then removed from the negatives, and autoclaved. PDMS wells were treated with 5% pluronic acid F127 solution (Sigma, P2443) for 1 hour before generating the 3D-EHTs.

hESC-CMs were cultured for ~ 21-24 days before 3D-EHTs generation. Flow cytometry was performed on the harvested cells using cTnT antibody (Thermo, MS-295-P) on a BD FACSCanto II instrument (Beckton Dickinson, San Jose, CA) and analysed using FACSDiva software (BD Biosciences), which revealed a purity of 90% ±0.5 (i.e., cTnT+). For 3D-EHTs generation, CMs and epicardial cells were

trypsinized and mixed in a collagen-based gel containing 10x RPMI-1640 medium (Sigma), NaOH, geltrex (Invitrogen, A1413202), collagen I Rat Protein (Gibco Life Technologies, A1048301) and water. The cell-gel mixture was poured into the PDMS wells and left to solidify for 30 minutes at 37°C. Each tissue contained either $5x10^5$ CMs alone or $5x10^5$ CMs plus $5x10^4$ supportive cells. Each tissue was fed with 7ml of RPMI media with B27 plus insulin every other day, and spontaneous contractions were observed within five days. All 3D-EHTs were cultured for 14 days prior to functional measurements as described below.

Frank-Starling force measurements of 3D-EHTs

Force measurement of 3D-EHTs were performed after two weeks in culture as previously described (Bargehr et al., 2019). These tissues were removed from the PDMS wells and suspended between a force transducer (Aurora Scientific, model 400A) and length controller (Aurora Scientific, model 312B). To examine its Frank-Starling active force generation, each tissue was stretched from its resting length to an additional 25% strain within 6 steps. Measurements were performed in a HEPES-buffered Tyrode solution at 37°C. Initially, force traces were recorded without electrical stimulation and subsequently with 1, 1.5, 2.5Hz at 5V and 50ms pulse duration. Both passive tension and active force traces were analysed with LabView and MATLAB software.

Non-ratiometric assessment of 3D-EHTs' calcium-handling

To analyse the tissues' calcium kinetics, the tissues were first incubated with Fluo-4 AM (Molecular Probes, Invitrogen) for 30 min at 37.5°C. Videos of constructs were recorded at intrinsic beating rates and paced at 1Hz, 1.5Hz and 2Hz with a Sony Handycam (Vixia HFS20) and fluorescence microscope (Nikon Eclipse TS100). Videos were taken at 60 frames per second (fps), converted to independent frames, imported, and analysed for fluorescence intensity per frame using Image J software. All videos were normalized to the background Ca^{2+} signal.

Histological processing of 3D-EHTs

Tissues were washed in PBS, fixed in 4% PFA for 60 minutes with subsequent embedding in 30% sucrose overnight at 4°C. This procedure is to reduce the tissue water content and improve tissue preservation during cryo-embedding. On the next

day, each tissue was fully embedded in OCT and transferred onto an ice bath composed of 100% ethanol on dry ice. Using a cryotome, the cryo-embedded blocks were serially sliced to produce sections with a 10μm thickness. To characterise hESC-CM, fibronectin deposition and integrin α5β1, antibodies directed at β-MHC (1:1 Developmental Studies Hybridoma Bank), FN (1:250, Abcam, Cat No: ab2413) and activated integrin α5β1 (1:200, Abcam, Cat No: ab150361) were used. Whole stained sections were scanned with Zeiss AxioScan 7. Subsequently, images were exported for further analyses of sarcomeric, and morphometric calculations as previously described (Liu et al., 2018, Bargehr et al., 2019, Wang et al., 2013, Ieda et al., 2009) via Image J software, performed in a blinded fashion.

pUR4 generation and cellular treatment

pUR4 is a small peptide derived from a surface protein of *Streptococcus pyogenes* termed F1 adhesin and is a well-described inhibitor of FN polymerization. pUR4 at ~99% purity was obtained commercially from Genscript. At D7 after epicardium differentiation, hESC-epicardium received pUR4 (500 nM) for 72hrs. During 3D-EHT casting, 10 uL of pUR4 (500nM) was included in the gel mixture, and similar concentration of pUR4 was added to the 3D-EHTs during alternative day media changes, for a total of 14 days.

Western blotting

After 72 hours of pUR4 treatment, fibronectin protein content was assessed by immunoblotting. Lysate from one confluent well of hESC-epi cells from a six-well plate was separated by SDS PAGE on an 8% acrylamide gel, using 10 ul of Precision Plus Protein All Blue as standards. Protein was then transferred overnight onto a polyvinylidene difluoride (PVDF) membrane (Merck Millipore, IPVH00010). Membranes were blocked with 5% fat-free milk in Tris-buffered saline and 0.05% Tween 20 (TBS-T) for 1 hour at room temperature, followed by incubation overnight at 4˚C. Primary antibodies used to detect fibronectin (1:250, Abcam ab2413) and to detect β-actin (1:1000, CST 2148S). Membranes were washed with TBS-T three times for 5 minutes at RT before incubation with secondary anti-rabbit (1:10,000 NEB 7074S) or anti-mouse (1:10,000 NEB 7076S) HRP-conjugated antibody for 1 hour at RT. Membranes were washed with TBS-T, and protein was detected with ECL western blotting detection reagents (Pierce).

Generation of CRISPR-Cas9-mediated Knockout Fibronectin (KOFN1) hESC cell Line

Crispr-Cas9-mediated knockout: annealing and cloning FN1-targeted sgRNA Oligonucleotides were designed using *homo sapiens FN1* sequences from Genscript (https://www.genscript.com/gRNA-database.html) and modified according to a Zhang Lab protocol (https://www.addgene.org/crispr/zhang/PX459-SpCas9+sgRNA). The sequence of the sgRNA was **(5' to 3')** CACCGTACAAACCAACGCATTGCCT with **(3' to 5')** CATGTTTGGTTGCGTAACGGACAAA. Oligonucleotides were annealed and ligated into the cut vector pSpCas9(BB)-2A-Puro (PX459) V2.0 (a kind gift from Feng Zhang) using T4 ligase for 1 hour at RT**.** The ligation mix was transformed into alpha-select competent cells (BioLine) and incubated prior to colony picking and sequencing.

Sequencing of transformed cells

Each colony of transformed cells was digested with the restriction enzyme BbsI to select out the cloned plasmids with sgRNA. Unmodified PX459V2 plasmid was used as a control. Colony digests were analysed by agarose gel (1%) electrophoresis (1.30 hour at 100V). Uncut plasmids showed a size of 580bp. Positive colonies were plasmid mini-prepped (Qiagen) before sequencing with Source BioScience. Plasmids with the correct insertion of the sgRNA sequence were midi-prepped (Qiagen).

Gene-targeting by GeneJuice-mediated transfection

Individual wells of hESCs were transfected with cloned plasmids using GeneJuice. After passaging, hESCs were incubated with 4 µg of DNA and 10 µl per well of GeneJuice in Opti-MEM medium (Gibco) for 24 hours. Cells were washed in PBS before incubation with DNA-OptiMEM mixtures. The DNA-OptiMEM mixtures comprised of (i) 4 µg DNA in 250 µl OptiMEM per well of a six-well plate and (ii)10 µl GeneJuice in 250 µl OptiMEM per well. 500 µl transfection mix of 1:1 of Mixture 1 & Mixture 2, was added to each well of hESCs. After 24 hours of incubation with DNA-OptiMEM mixtures, cells were cultured in mTeSR. After 2 days, 1 µg/ml puromycin-enriched culture media was added to the cells and puromycin-resistant colonies were picked for expansion.

Genotyping of targeted clones

Genomic PCR was used to screen genetically targeted clones to verify site-specific targeting, determine whether allele targeting was heterozygous or homozygous, and to check for off-target integrations of the targeting plasmid. Sequences of FN1 primer stated in **Supplemental Table 1**.

***FN1* Primer name**	**FWD Sequence (5' to 3')**	**RVS Sequence (5' to 3')**
*FN1*_exon2_1	ATGTGACTTCAATTGTCTGCCTTC	CTCGCAGTTAAAACCTCGGCT
*FN1*_exon2_2	TGGGAAAAGGAGAAATGCAAATGTA	AACTATGGGGCTTGTTGTCAC
*FN1*_exon3_1	GTGGGTTTTCCTTTAGAGGGGATT	CCTTACTTGCGATGGTACAGC
*FN1*_exon3_2	ACCGAGTGGGTGACACTTATG	GGCAAACCTCAAAGTTCGGA
*FN1*_exon4_1	CATGAAGGGGGTCAGTCCTAC	TGTAGATGTGATTCTGGTCCAACC
*FN1*_exon4_2	CGTTGTATCTTCAACAGACCGC	CTGGTCCAACCCCACATTAGAA

SUPPLEMENTAL TABLE 1: PCR PRIMER SEQUENCES FOR GENOTYPING CRISPR-CAS9-EDITED KOFN CLONES

Briefly, confluent colonies were used for genomic DNA extraction (Qiagen) and genomic PCR with *FN1*-specific primers were done. The genomic DNA was sent for Sanger sequencing with either FWD or RVS *FN1*-specific primers. One homozygous-targeted clone for each vector transfection was selected for subsequent differentiation into hESC-epicardium.

Generation of Inducible Fibronectin Knockdown (sOPTiKD-FN) hESC cell line

Inducible knockdown: design and annealing shRNA oligonucleotides

For generation of an inducible Fibronectin knockdown (sOPTiKD-FN1) hESC cell line, an shRNA was selected from the Broad Institute TRC library (Moffat et al., 2006). The shRNA sequences for psOPTIkd vector construction used: TOP (5' to 3') GATCCCGCCTGCTCCAAGAATTGGTTTCTCGAGAAACCAATTCTTGGAGCAGGC

TTTTTTG and BOTTOM (5' to 3') TCGACAAAAAAGCCTGCTCCAAGAATTGGTTTCTCGAGAAACCAATTCTTGGAG CAGGCGG. BglII overhang is in red, terminator sequence/SalI overhang in blue. Oligonucleotides were annealed as previously described (22), and ligated into the linearised, optimised inducible knockdown sOPTiKD vector (a gift from the Vallier Group, University of Cambridge) using T4 ligase for 2 hs at room temperature. The ligation mix was transformed into alpha-select competent cells (BioLine), prior to colony PCR screening for successful transformants.

Colony PCR of transformants

After overnight incubation, transformants grown on LB agar plates were picked in the morning for colony PCR to check for transformation. AAVs-KD forward (CGAACGCTGACGTCATCAACC) and reverse (GGGCTATGAACTAATGACCCCG) primers were used; thermocycling conditions were as follows: 95°C for five minutes, then 35 cycles of 95°C for 30 seconds, 63°C for 30 seconds and 72°C for 1 minute. These PCR reactions were analysed by agarose gel (1.5%) electrophoresis; vectors with the desired insert showed a size of 520bp. Miniprep of transformed colonies (Qiagen, miniprep kit) were conducted for genomic DNA extraction before Sanger sequencing. Sequencing was done via Source BioScience with the protocol specified for strong hairpin structures. Plasmid vectors with a correctly inserted shRNA sequence were expanded and selected for Midiprep (Qiagen), in preparation for cell transfection.

Gene-targeting by GeneJuice-mediated transfection

To generate an inducible *FN1* knockdown hESC cell line, AAVS1 locus targeting was performed by GeneJuice-mediated transfection. Briefly, individual wells of hESCs were transfected with five different cloned plasmids using GeneJuice. After passaging, hESCs were incubated with 4 µg of DNA and 10 µl per well of GeneJuice in Opti-MEM medium (Gibco) for 24 hours. Cells were washed in PBS before incubation with DNA-OptiMEM mixtures. The DNA-OptiMEM mixtures comprised of (i) 4 µg DNA in 250 µl OptiMEM per well of a six-well plate and (ii)10 µl GeneJuice in 250 µl OptiMEM per well. The mixtures were mixed gently and incubated at room temperature for 5 minutes. 250 µl of Mixture 2 was then added to 250 µl Mixture 1 before incubation at room temperature for 20 minutes.

500 µl transfection mix of 1:1 of Mixture 1 & Mixture 2, was added to each well of hESCs. After 24 hours of incubation with DNA-OptiMEM mixtures, cells were cultured in mTeSR. After 2 days, 1 µg/ml puromycin-enriched culture media was added to the cells. A week later, puromycin-resistant colonies were picked and expanded.

Genotyping of targeted clones

Genomic PCR was used to screen genetically targeted clones to verify site-specific targeting and determine whether allele targeting was heterozygous or homozygous. PCR primers used as in **Supplemental Table 2**. Locus PCR ('PCR 1') for wild-type AAVS1 locus indicates a non-targeted allele. 'PCR 2' is a locus PCR/loss-of-allele PCR. 'PCR 2' and 'PCR 3' refer to 5'INT/3'INT PCR respectively, which are PCR reactions for vector backbone 5'-end and 3'-end genomic integration region, indicative of specific transgene targeting.

Primer name	**PCR Type**	**Primer Sequence**
AAVS1_Genomic_FWD	Locus ('1')	CTGTTTCCCCTTCCCAGGCAGGTCC
AAVS1_Genomic_REV	Locus ('1')	TGCAGGGGAACGGGGCTCAGTCTGA
AAVS1_Genomic_FWD	5' Integration into AAVS1 ('2')	CTGTTTCCCCTTCCCAGGCAGGTCC
AAV_Pur_REV	5' Integration into AAVS1 ('2')	TCGCGCGGGTGGCGAGGCGACCG
OPT_tetR_FWD	3' Integration into AAVS1 ('3')	CCACCGAGAAGCAGTACGAG
AAVS_Genomic_REV	3' Integration into AAVS1 ('3')	TGCAGGGAACGGGGCTCAGTCTGA

SUPPLEMENTAL TABLE 2: PCR PRIMER SEQUENCES FOR GENOTYPING SOPTIKD CLONES

Firstly, DNA was extracted from all targeted clones using a genomic DNA extraction kit (Sigma-Aldrich). All PCRs were performed using 100 ng of genomic DNA as a template in a 25 µl reaction volume, LongAmp Taq DNA Polymerase (NEB), and

including 2.5% (v:v) dimethyl sulphoxide (DMSO). One homozygous-targeted clone for each vector transfection was selected for subsequent differentiation into hESC-epicardium with or without the addition of 1 μg/ml tetracycline (Sigma) to culture media with the aim of mediating *FN1* knockdown. hESC-epicardium was differentiated in the presence and absence of tetracycline.

Statistics

All *in vitro* studies were performed as three biological replicates (independent experiments) from different cellular differentiations. Statistical testing was performed using an unpaired t-test for two-group comparisons and a paired t-test for comparison of two paired groups. One-way ANOVA was used for the statistical comparison of more than two groups, and a post-hoc Tukey test was used if the group variance was equal. As for groups with unequal variance, a post-hoc Kruskal–Wallis test with Dunn's correction for multiple comparisons was applied. Measuring two-sided significance, a *P*-value of 0.05 was considered statistically significant. All results are presented as mean ± s.e.m unless otherwise stated. All analyses were performed using GraphPad Prism 9.0 software.

Bulk RNA sequencing

The starting material for RNA sequencing was H9 hESC-EPIs, H9 hESC-neural crest cells (hESC-NCs) and H9 hESC-CMs, and undifferentiated H9s. HESC-EPIs were differentiated from H9s via early and lateral mesoderm induction, prior to differentiation to epicardium as previously described (Bargehr et al., 2019, Iyer et al., 2015). HESC-NC was differentiated from H9s as previously described (Bargehr et al., 2019). HESC-CMs were differentiated as monolayers with a commercially available kit (Thermo Fisher Scientific) (Liu et al., 2017). Day 30 hESC-CMs were used for all further bioinformatics analysis. The datasets had previously been deposited in the NCBI's Gene Expression Omnibus under accession number GSE122714 for hESC-EPI and hESC-NC and GSE85331 for the hESC-CM and hESC-EPI (Bargehr et al., 2019).

Raw FASTQ files of the hESC-CM and H9 datasets were downloaded from the European Nucleotide Archive (ENA) under the run accession identifiers SRR4011898, SRR4011899, SRR4011904 and SRR4011905. The FASTQ files were preprocessed using fastp, with the default parameters (fastp). Transcript-level counts

for the paired files were estimated using the pseudoalignment tool kallisto (Bray et al., 2016) using the full list of cDNA contained in the annotated Homo sapiens genome (version GRCh38 release 98). Transcripts were merged by gene ensembl identifier to produce gene-level features ready for further analysis.

As described more fully in (Bargehr et al., 2019), the hESC-EPI and hESC-NC data were mapped to the Homo sapiens genome GRCh38 using HISAT2 (Kim et al., 2015). Reads were counted using SeqMonk (https://www.bioinformatics.babraham.ac.uk/projects/seqmonk/) and were already locally available; these steps were not repeated for this analysis and we used the same counts matrix that was generated in (Bargehr et al., 2019).

Both read count matrices were imported in R and processed to remove low expression genes. As no comparisons were made between datasets the analysis was run in parallel and an intersection of the features was not created. The technical validation of both datasets is as displayed in **Supp Figure 4**.

Analysis of Epicardial-Myocardial Interactome

Workflow to generate the epicardial-myocardial interactome

To identify the molecular pathways by which hESC-EPIs improved hESC-CM's structure and function, the interface of secreted hESC-EPI factors and membrane-bound cell surface receptors on hESC-CMs were investigated.

We first performed a differential expression analysis between the hESC-EPI and hESC-NC, using DESeq2. As previously described, hESC-NCs were chosen as a negative control due to their redundancy in hESC-CM maturation and development (Bargehr et al., 2019). The list of differentially upregulated genes was filtered to retain only genes encoding putatively secreted proteins according to the Human Protein Atlas (http://www.proteinatlas.org/humanproteome/secretome) (Uhlén et al., 2019). This dataset is entitled as the hESC-EPI secretome (**Fig 5**). In parallel, differential expression analysis was performed between day 30 hESC-CM and H9s before differentiation. The list of differentially expressed genes was filtered and restricted to genes encoding receptors and proteins with predicted membrane- anchored regions according to the Human Protein Atlas (Uhlén et al., 2019). This dataset is termed the

hESC-CM membranome (**Fig.5**). We found a potential secretome of 379 upregulated factors and a membranome of 1417 upregulated receptors (**Fig.5**).

Next, to determine the interactome, both gene lists were jointly analysed to elucidate hESC-EPI secreted factors and their respective membrane-bound receptors on hESC-CMs.

We used the interaction database StringDB v11 (https://string-db.org/cgi/download.pl [2019 11 29]) which covered 99.5 % and 95.5 % of the upregulated secretome and membranome genes respectively. We constructed the interactome by filtering the secretome to retain genes with interactions with genes found only within the membranome. Initially, we only included high-confidence interactions with an experimental evidence score of above 700. However, to uncover further potential interactions and generate a more cohesive interactome network within the high-confidence interactome, we included a set of lower-score interactions with a minimum score of 400. The interactome network is shown in (**Fig.5)**.

If a secreted protein was equally or greater expressed by hESC-CM than by hESC-EPI, then it is unlikely this would mediate the beneficial effects of hESC-EPIs on the other cell type. Since the aim of this study was to identify putative factors that mediate the positive effects of hESC-EPI, the interactome network was filtered to retain only interactions where the expression of secreted protein transcripts was significantly higher in the hESC-EPIs when compared to hESC-CMs ($p < 0.05$) (**Fig. 5**). To relate these molecular pathways to cardiac repair, the interactome was categorised into separate groups using the following biological process terms cardiomyocyte proliferation, maturation, survival, angiogenesis, development, extracellular matrix (ECM) regulation, inflammation, metabolism and regeneration. This functional annotation was performed manually following a review of the literature of all presented gene pairs and one or more regenerative biological processes were attributed to interactions based on previously identified signalling pathways. The literature used for this decision process is listed in **Table 1**.

Technical Validation of sequenced data

To validate technical aspects of sequencing before analysis, read counts for both datasets were sub-sampled at different levels to generate theoretical gene detection saturation curves **Supp Figure 4.** Although higher depths of sequencing are

generally observed with bulk RNAseq analyses, the number of genes detected appeared to plateau across all samples. This suggests that the transcriptional complexities of the cell lines were efficiently captured, confirming that the sequencing depth of all cell lines was adequate for further analysis.

Technical Validation of epicardial and cardiomyocyte differentiation

H9s were differentiated to lateral mesoderm and subsequently to epicardium phenotype as previously described (Bargehr et al., 2019, Iyer et al., 2015) Cells were subsequently prepared for RNA sequencing as previously described (Bargehr et al., 2019). Confirmation of cell line phenotypes was carried out by testing for differences in the expression of key markers. The expressions of key epicardial cell markers such as *WT1*, *ALDH1A2, TCF21,* and *BNC1* were increased in the H9 hESC-EPI samples when compared with H9 hESC-NC while the neural crest markers *SOX9* and *TFAP2A* were also seen to be lower in H9 hESC-EPI samples than in H9 hESC-NC (**Fig. 5**).

H9s were differentiated to cardiomyocyte phenotype with a commercially available differentiation kit as detailed and were sequenced on day 30 of differentiation as previously described (Liu et al., 2017). The expressions of the key cardiomyocyte markers *MYH6, MYH7, MYL2* and *MYL7* were significantly higher in the D30 H9 hESC-CM samples than in the H9 samples. Moreover, the expressions of pluripotent markers *SOX2* and *POU5F1* (*OCT4*) were reduced from D0 to D30 in the H9 hESC-CM data set (**Fig. 5**).

These differences were significant in all cases and were determined with a Welch's two samples t test ($p < 0.05$). Finally, isogenic replicates were highly correlated. The lowest correlation within replicates was seen between H9 hESC-NC samples (Spearman's Rho > 0.895, not shown). The cell lines used in constructing our interactome were thus deemed technically valid in terms of the quality and congruency of data, and as *bona fide* H9-derived versions of the human tissues in question.

The code used to generate and process the interactome in this manuscript has been deposited on GitHub (https://github.com/Hindrance/EpiSciData2020).

References

Liu YW, Chen B, Yang X, Fugate JA, Kalucki FA, Futakuchi-Tsuchida A, et al. Human embryonic stem cell-derived cardiomyocytes restore function in infarcted hearts of non-human primates. Nature biotechnology. 2018;36(7):597-605.

Bargehr J, Ong LP, Colzani M, Davaapil H, Hofsteen P, Bhandari S, et al. Epicardial cells derived from human embryonic stem cells augment cardiomyocyte-driven heart regeneration. Nature biotechnology. 2019;37(8):895-906.

Wang J, Karra R, Dickson AL, Poss KD. Fibronectin is deposited by injury-activated epicardial cells and is necessary for zebrafish heart regeneration. Developmental biology. 2013;382(2):427-35.

Ieda M, Tsuchihashi T, Ivey KN, Ross RS, Hong TT, Shaw RM, et al. Cardiac fibroblasts regulate myocardial proliferation through beta1 integrin signaling. Dev Cell. 2009;16(2):233-44.

Iyer, Dharini, Laure Gambardella, William G Bernard, Felipe Serrano, Victoria L Mascetti, Roger a Pedersen, Amarnath Talasila, and Sanjay Sinha. 2015. “Robust Derivation of Epicardium and Its Differentiated Smooth Muscle Cell Progeny from Human Pluripotent Stem Cells.” Development (Cambridge, England) 142 (8): 1528–41. https://doi.org/10.1242/dev.119271

Bertero, Alessandro, Matthias Pawlowski, Daniel Ortmann, Kirsten Snijders, Loukia Yiangou, Miguel Cardoso De Brito, Stephanie Brown, et al. 2016. “Optimized Inducible ShRNA and CRISPR/Cas9 Platforms for in Vitro Studies of Human Development Using HPSCs.” Development (Cambridge) 143 (23): 4405–18. https://doi.org/10.1242/dev.138081.

Kim, Daehwan, Ben Langmead, and Steven L. Salzberg. 2015. “HISAT: A Fast Spliced Aligner with Low Memory Requirements.” Nature Methods 12 (4): 357–60. https://doi.org/10.1038/nmeth.3317

Liu Q, Jiang C, Xu J, Zhao MT, Van Bortle K, Cheng X, et al. Genome-Wide Temporal Profiling of Transcriptome and Open Chromatin of Early Cardiomyocyte Differentiation Derived From hiPSCs and hESCs. Circulation research. 2017;121(4):376-91

Moffat J, Grueneberg DA, Yang X, Kim SY, Kloepfer AM, Hinkle G, Piqani B, Eisenhaure TM, Luo B, Grenier JK, Carpenter AE, Foo SY, Stewart SA, Stockwell BR, Hacohen N, Hahn WC, Lander ES, Sabatini DM, Root DE. A lentiviral RNAi library for human and mouse genes applied to an arrayed viral high-content screen. Cell. 2006 Mar 24;124(6):1283-98. doi: 10.1016/j.cell.2006.01.040.

Uhlén M, Karlsson MJ, Hober A, Svensson AS, Scheffel J, Kotol D, et al. (2019). The human secretome. Sci Signal, 12, 609

Bray NL, Pimentel H, Melsted P, Pachter L. Near-optimal probabilistic RNA-seq quantification. Nature biotechnology. 2016;34(5):525-7.